学位論文（要約）

Ultrafast nonlinear optical responses of Landau-quantized graphene in the terahertz range

(ランダウ量子化した単層グラフェンの
テラヘルツ帯超高速非線形光学応答)

平成28年度12月博士（理学）申請

東京大学　大学院理学系研究科
物理学専攻
湯本 郷

Abstract

Graphene, a single atomic layer of carbon atoms forming a honeycomb lattice structure, hosts a unique two-dimensional electron system consisting of massless relativistic particles, i.e., massless Dirac fermions, originating from the linear energy dispersion in the low-energy regime. When a strong magnetic field (B) is applied perpendicularly to graphene, in sharp contrast to the equidistant Landau levels (LLs) in ordinary two-dimensional electron gas (2DEG), the energy spectrum is separated into non-equidistant LLs with the $\sqrt{B}$-proportional energy spacing in the terahertz (THz) and mid-infrared range. In addition to the peculiar transport properties such as half-integer quantum Hall effect (HIQHE), the optical responses of Landau-quantized graphene have attracted great interest. For instance, magneto-optical spectroscopy studies have revealed intriguing linear magneto-optical responses in the THz and mid-infrared range such as the unusual optical transition selection rule between the LLs, and quantum Faraday and Kerr effects in quantum Hall regime which are the optical analogue of HIQHE. Recently, in addition to the magneto-optical properties in the linear response regime, the non-equilibrium dynamics of the LLs in graphene such as the carrier relaxation has been investigated by means of pump-probe spectroscopy.

The optical transition dipole moments between LLs are characterized by el_{B}, where l_{B} is the magnetic length, and become so large that the extreme nonlinear optics regime, where the maximum Rabi frequency exceeds the carrier frequency of the light pulse, can be realized with feasible electric field strength. In such a non-perturbative light-matter interaction regime, a number of fascinating phenomena are expected such as carrier-wave Rabi flopping and high-order harmonic generation. However, in the ordinary 2DEG system, the optical nonlinearity is absent due to the harmonic energy spectrum of the equidistant LLs. In this sense, in addition to its peculiar linear optical responses, Landau-quantized graphene is expected to be a very fascinating nonlinear optical material with its inherent anharmonicity according to the non-equidistant energy spectrum arising from the relativistic nature of electrons.

In this dissertation, we first perform single pulse transmission experiments with intense THz pulses on a monolayer epitaxial graphene under strong magnetic fields. From the measurements of the Faraday rotation angle and ellipticity spectra, the suppression of the Faraday rotation is observed with increasing the intensity of the incident THz

pulse. To further investigate the nonlinear THz responses of the non-equidistant LLs in graphene, we perform THz pump-THz probe magneto-optical spectroscopy and observe the ultrafast suppression and recovery of the Faraday rotation under the intense off-resonant THz pulse excitation, where the maximum Rabi frequency far exceeds the carrier wave frequency of the excitation THz pulse and even larger than the relevant LL transition frequency. In order to analyze the experimental results, we perform numerical simulations of the nonlinear responses of the LLs based on the master equation for the density matrix elements without using rotating-wave approximation and discuss the microscopic mechanism of the THz nonlinearity observed in the pump-probe experiments. Finally, we propose the higher harmonic generation from Landau-quantized graphene, which emerges in the extreme nonlinear optics regime, based on the numerical simulations and examine the feasibility of the experiments.

Contents

1 Introduction **1**
- 1.1 Large optical nonlinearity of graphene under zero magnetic field 1
- 1.2 Magneto-optical spectroscopy of graphene 3
- 1.3 Motivation 6
- 1.4 Structure of the dissertation 7

2 Properties of graphene **8**
- 2.1 Electronic properties of graphene 8
- 2.2 Landau quantization of Dirac electrons in graphene 10
- 2.3 Optical properties of the non-equidistant LLs in graphene 14
  - 2.3.1 Optical transition selection rule 14
  - 2.3.2 Giant dipole moment matrix elements between LLs 15

3 Principles of polarization-resolved THz spectroscopy **18**
- 3.1 Terahertz time-domain spectroscopy (THz-TDS) 18
  - 3.1.1 THz generation 18
  - 3.1.2 THz detection 20
  - 3.1.3 Experimental setup for THz-TDS 23
- 3.2 THz magneto-optical spectroscopy 25
  - 3.2.1 Faraday rotation and description of polarization state 25
  - 3.2.2 Faraday rotation in graphene 26
  - 3.2.3 Polarization detection technique 29

4 Experimental techniques **31**
- 4.1 Sample 31
- 4.2 Laser source 33
- 4.3 Single pulse transmission experiment 33
- 4.4 THz pump-THz probe magneto-optical spectroscopy 35
  - 4.4.1 Experimental setup 35
  - 4.4.2 Measurement of THz pump-THz probe signals 42

5 Observation of ultrafast nonlinear THz responses in Landau-quantized graphene **46**
5.1 Single pulse transmission experiment 46
5.2 THz pump-THz probe magneto-optical spectroscopy 51
5.2.1 Experimental conditions 51
5.2.2 Ultrafast nonlinear THz responses under the intense pump THz pulse 53
5.2.3 Pump-induced optical conductivity change: drastic LL-ladder climbing of electrons 55

6 Numerical simulations based on the density matrix formalism **60**
6.1 Master equation for nonlinear THz responses of Landau-quantized graphene 60
6.2 Simulations of nonlinear Faraday rotation observed in the single pulse transmission experiments 64
6.3 Simulations of THz pump-THz probe signals 67
6.3.1 Nonlinear THz responses and a drastic population redistribution . 68
6.3.2 Macroscopic polarizations between the LLs 73
6.4 Towards the observation of higher harmonics 79

7 Conclusion and outlook **85**
7.1 Conclusion 85
7.2 Outlook 86

References **87**

Chapter 1

Introduction

1.1 Large optical nonlinearity of graphene under zero magnetic field

Electrons in graphene, one atomic layer of carbon atoms forming a honeycomb lattice structure, behave like massless relativistic particles, i.e., massless Dirac fermions, due to the linear energy dispersion in the low-energy regime. The Dirac electron nature gives rise to a number of fascinating phenomena such as Klein tunnelling [1, 2] and the half-integer quantum Hall effect [3, 4]. In addition to these unique transport properties, graphene has attracted growing interests from photonics and optoelectronics because of its intriguing optical responses [5, 6]. In particular, graphene is expected to host a large optical nonlinearity in the mid-infrared to the visible [7, 8] and the terahertz (THz) [9] ranges, which arises from the linear energy dispersion of the relativistic electrons. Because the linear band structure makes the interband optical transitions resonant over a wide range of photon energy corresponding to the mid-infrared to the visible range, the third-order optical nonlinearity becomes remarkably large, which has been experimentally observed by the measurements of the coherent nonlinear optical responses such as four-wave mixing [7] and third-harmonic generation [10, 11] as schematically shown in Fig. 1.1.

The large optical nonlinearity is also expected to appear in the THz range, where the intraband response plays a dominant role, because the linear band dispersion makes the intraband response anharmonic unlike the quadratic dispersion. This nonlinearity can be intuitively understood in a simplified picture as follows [9] (Fig. 1.2). Considering the Newton equation of motion $dp_x/dt = -eE_x(t)$ (e is the elementary charge) with the external electric field $E_x(t) = E_0 \cos \Omega t$, we obtain $p_x = -(eE_0/\Omega) \sin \Omega t$. In graphene, the velocity v_x is written by

$$v_x = v_{\mathrm{F}} \frac{p_x}{\sqrt{p_x^2 + p_y^2}}, \tag{1.1}$$

where v_{F} is the Fermi velocity. Equation (1.1) is reduced to $v_x \sim v_{\mathrm{F}} p_x/|p_x| = v_{\mathrm{F}} \mathrm{sgn}(p_x)$

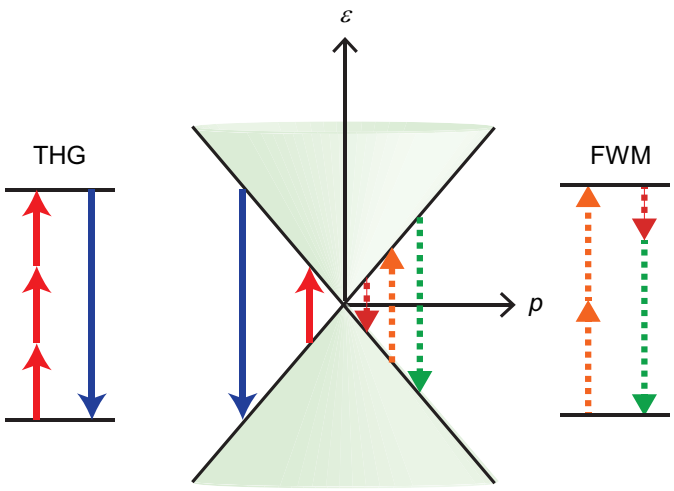

Figure 1.1: Band structure of graphene with resonant photon energies (arrows) appearing in energy-level diagrams describing third-harmonic generation (THG) and four-wave mixing (FWM).

when we assume $p_y \sim 0$. Therefore, the ac electric current $j_x = -envx$ (n is the area density of carriers) can be written by

$$\begin{aligned} j_x(t) &= env_{\mathrm{F}}\mathrm{sgn}(\sin\Omega t) \\ &= env_{\mathrm{F}}\frac{4}{\pi}\left(\sin\Omega t + \frac{1}{3}\sin 3\Omega t + \frac{1}{5}\sin 5\Omega t + \ldots\right), \end{aligned} \tag{1.2}$$

which clearly shows nonlinear nature of graphene showing up in the low frequency THz range.

Recently, the nonlinear optical responses to intense THz light have been intensively investigated both theoretically [12–14] and experimentally [15–18]. The observation of the third- and fifth-harmonic generation has been reported for a 45-layer graphene sample [15], whereas other high-field THz spectroscopies on single [16–18] and ∼10-layer [16] graphene samples have detected no harmonic generation and observed the nonlinear suppression of the optical conductivity. The suppression of the optical conductivity has recently been found to be described by statistically determined thermodynamic picture because of fast electron thermalization [18]. Therefore, further studies are expected to clarify when the coherent process dominates over the fast thermalization effect in the nonlinear optical responses in the THz frequency range.

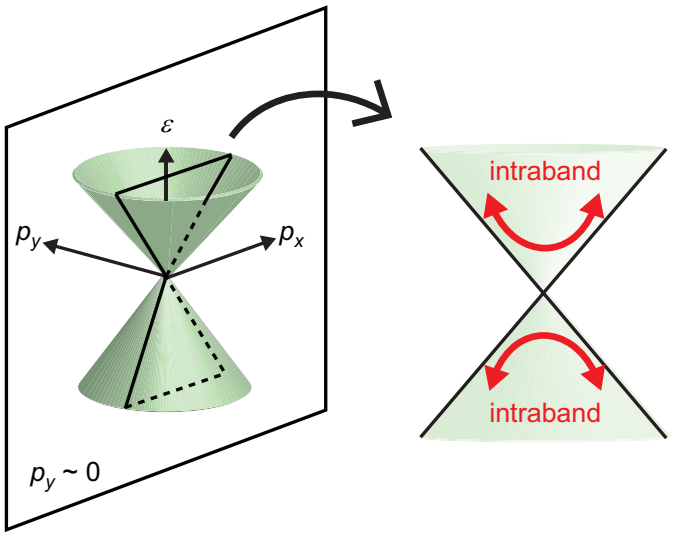

Figure 1.2: Schematic of the anharmonic intraband dynamics of Dirac electrons in the vicinity of $p_y = 0$.

1.2 Magneto-optical spectroscopy of graphene

When a strong magnetic field is applied perpendicularly to graphene, unlike the equidistant Landau levels (LLs) in ordinary two-dimensional electron gas (2DEG), the energy spectrum is separated into LLs with non-equidistant energy spacing covering the THz and mid-infrared ranges. The non-equidistant LL energies are given by

$$\epsilon_n = \mathrm{sgn}(n) v_\mathrm{F} \sqrt{2|e|\hbar B|n|}, \tag{1.3}$$

where n ($n = 0, \pm 1, \pm 2 \cdots$) is the LL index and B is the magnetic field [19]. The peculiar electronic properties have attracted great interest to study magneto-optical responses of graphene and the unique optical responses in the THz and mid-infrared ranges have been revealed in the linear response regime [20–25]. In the linear response regime, the induced surface current density j is proportional to the driving electric field E:

$$j_i = \sigma_{ij} E_j, \tag{1.4}$$

where the subscripts i and j denote Cartesian components and σ_{ij} is the linear optical conductivity which is independent of the driving electric field. In a high-doped monolayer graphene sample with the Fermi energy of $E_\mathrm{F} \sim 350$ meV, Crassee *et al.* observed giant Faraday rotation with the maximum Faraday rotation angle of > 100 mrad for just a single atomic layer [20], which was well explained by the Drude model. In addition to such magneto-optical responses in the classical regime, where the separation between the LLs is not clearly established due to the LL broadening, the THz responses in the

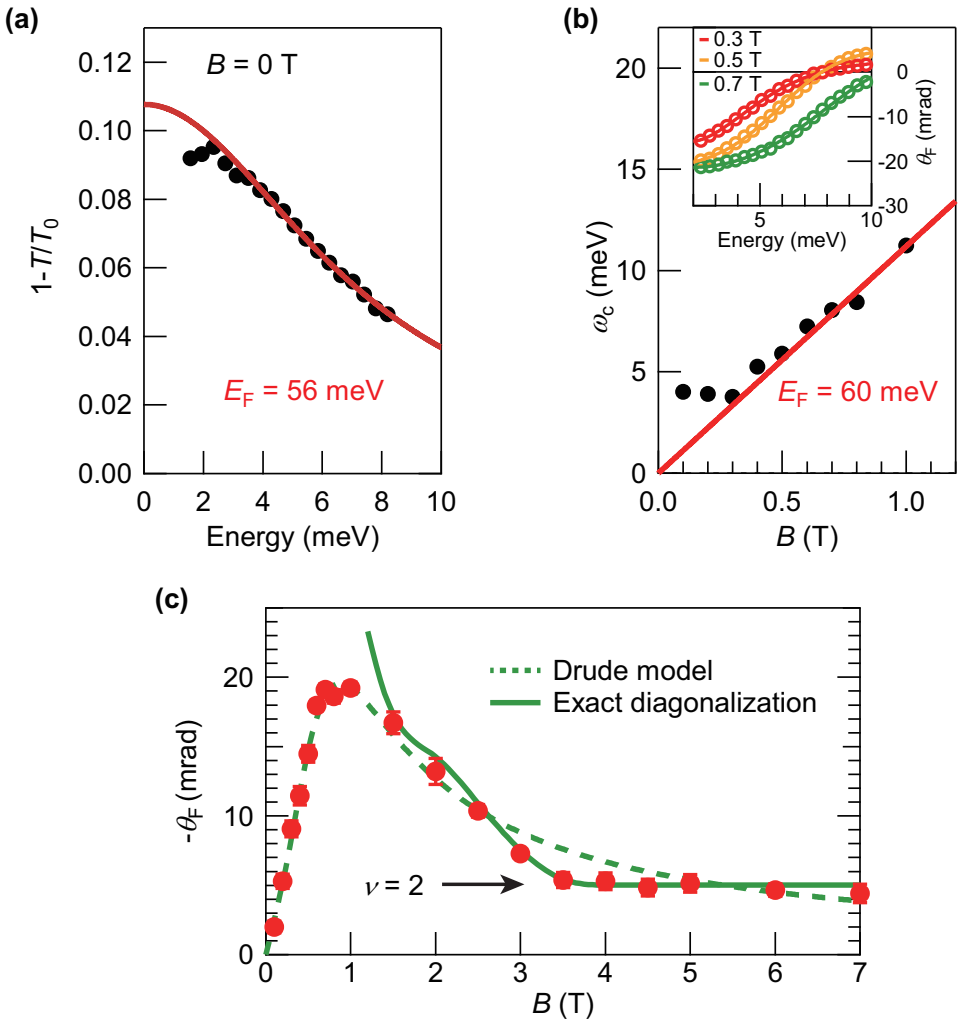

Figure 1.3: (a) Absorption spectrum of epitaxially-grown monolayer graphene at zero magnetic field in the THz frequency range. The red curve is the Drude fit with $E_{\mathrm{F}} = 56$ meV. (b) Cyclotron frequencies as a function of the applied magnetic field obtained from the Drude fits to the Faraday rotation spectra under weak magnetic fields as shown in the inset. The red solid line is calculated with $E_{\mathrm{F}} = 60$ meV. Inset: The Faraday rotation spectra at $B = 0.3$, 0.5, and 0.7 T with the Drude fits (solid curves). (c)Magnetic field dependence of the Faraday rotation angle at the photon energy of 4 meV (~ 1 THz). The dashed and solid curves are calculated by the Drude model and the exact diagonalization method, respectively, both of which are multiplied by a reduction factor of 0.7. From ref. [21].

quantum Hall regime have been observed by Shimano *et al.* with a monolayer graphene epitaxially grown on the Si face of a SiC substrate [21]. The Fermi energy of the sample was estimated to be $E_{\rm F} = 56$ meV from the Drude fit of the absorption spectrum measured at zero magnetic field as shown in Fig. 1.3 (a). As shown in the inset of Fig. 1.3 (b), the Faraday rotation spectra under weak magnetic fields are also well fitted by the Drude model. From the slope of the linear dependence of the obtained cyclotron frequencies on the applied magnetic field above 0.4 T (the deviation below 0.3 T is most likely attributed to the existence of the magnetoplasmons [26]) $E_{\rm F}$ is estimated to be 60 meV, which agrees well with the value obtained from the Drude fit to the THz transmittance spectrum under zero magnetic field. In this low-doped sample, the quantum Hall regime was realized above 3 T. The plateau structure is observed in the magnetic field dependence of the Faraday rotation angle at the photon energy of 4 meV ($\sim$ 1 THz) as shown in Fig. 1.3 (c). The plateau region corresponds to the filling factor of $\nu = 2$, and the rotation angle is defined by the fine structure constant. The magnetic field dependence of the Faraday rotation angle is well reproduced by an exact diagonalization method which takes into account the localization effect. The absolute value of the rotation angle is multiplied by a factor of 0.7 in order to fit to the experimental results, which is most likely attributed to a $\sim 80\%$ coverage of monolayer graphene.

In addition to the linear magneto-optical spectroscopy, time-resolved spectroscopies have been performed and the carrier relaxation dynamics of LLs in graphene has been investigated [27–29]. Plochocka *et al.* performed a degenerate pump-probe experiment with 800-nm-wavelength laser pulses. They observed the increase of the relaxation time for LLs with a high LL index ($n \sim 100$), which was attributed to the suppression of Auger relaxation processes [27], arising from the energy mismatch $\delta\epsilon$ in the Auger processes between the adjacent LLs described by

$$\delta\epsilon = \mathrm{sgn}(n) v_{\rm F} \sqrt{2|e|\hbar B}(2\sqrt{n} - \sqrt{n+m} - \sqrt{n-m}), \tag{1.5}$$

with $n, m > 0$, which is schematically shown in Fig. 1.4. In addition to the above study [27] of carrier dynamics in the high-n-LLs with the non-equidistant spacing, the investigation on the carrier dynamics has been made by Mittendorff *et al.* [29]. They studied the carrier dynamics of low LLs ($n = 0, \pm 1$), which can be considered to be decoupled from the other LLs in their experiment, by degenerate THz pump-probe spectroscopy using a free-electron laser light source with a frequency of 18 THz. From the differential transmission signals, they observed strong Auger processes between the equidistant LLs with $n = -1$, 0 and 1. In contrast to such studies on the population dynamics of carriers in the LLs, the coherent nonlinear optical responses in the Landau-quantized regime remain unexplored.

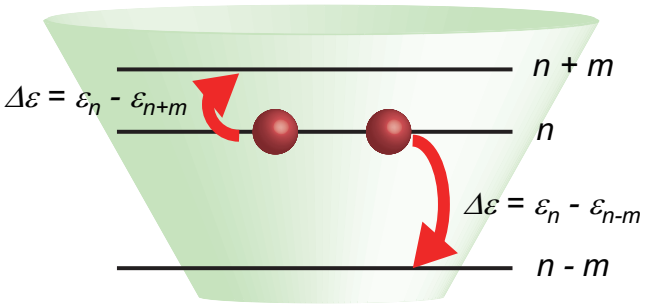

Figure 1.4: Schematic of the energy mismatch for the Auger processes between $(n-m)$-th, n-th and $(n+m)$-th LLs.

1.3 Motivation

In 2DEG systems, the cyclotron orbits are confined within the two-dimensional plane with the radii on the order of the magnetic length l_{B}. Therefore, the optical transition dipole moments between LLs are characterized by el_{B} [30] and become so large that the extreme nonlinear optics regime, where the Rabi frequency $\Omega_{\mathrm{R}} = \mu E/\hbar$ (μ is the transition dipole moment and E is the electric field strength) exceeds the carrier frequency of the light pulse, can be realized with feasible electric field strength in the THz range. In such a strong light-matter coupling regime, the perturbation theory breaks down and a number of fascinating phenomena emerge such as carrier-wave Rabi flopping [31], high-order harmonic generation (HHG), and attosecond pulse generation [32]. Recent developments of carrier-envelope-phase-locked intense THz and mid-infrared light sources have enabled such a study even in solid states, as exemplified by sub-cycle coherent control of electrons [33] and HHG in semiconductors [34, 35]. In these experiments, however, ultra-intense electric fields of ~ 10 MV/cm were needed to explore such nonlinear optical phenomena. In this sense, a Landau-quantized 2DEG system may offer a unique condensed-matter playground to study the non-perturbative light-matter interaction phenomena with relatively weak electric fields owing to the large dipole moments. However, in ordinary 2DEG systems with equidistant LLs, the optical nonlinearity is absent unless one introduces anharmonicity into the system, e.g., the non-parabolic electron band dispersion and electron-ion interaction effect [36]. In contrast, the LLs in graphene intrinsically show anharmonicity according to the non-equidistant energy spectrum, reflecting the relativistic nature of electrons. Indeed, the coherent nonlinear optical responses of graphene in the Landau-quantized regime have attracted many theoretical interests [37–39].

In spite of such large optical nonlinearities, the coherent nonlinear optical responses of Landau-quantized graphene still remain unexplored. In this dissertation, we aim to reveal the nonlinear optical responses in the THz range under strong light-matter coupling regime and propose the possibility to study the extreme nonlinear optics phenomena in

solid state materials with relatively weak electric fields on the order of several tens of kV/cm.

We developed a THz pump-THz probe magneto-optical spectroscopy system under the strong magnetic fields. We studied the ultrafast nonlinear magneto-optical responses of Landau-quantized graphene under the irradiation of intense off-resonant THz pulse, where the maximum Rabi frequency far exceeds the carrier wave frequency of the pump THz pulse and even larger than the relevant LL transition frequency. To analyze the experimental results, we performed numerical simulations of the nonlinear optical responses of the LLs based on the density matrix formalism without using rotating-wave approximation. Finally, with using the simulations, we investigated the experimental feasibility for the detection of the higher harmonic generation from the non-equidistant LLs in graphene under the irradiation of multicycle THz pulses.

1.4 Structure of the dissertation

This dissertation is structured as follows. In chapter 2, we review the electronic properties of graphene with and without an external magnetic field and then introduce the unique optical properties of the non-equidistant LLs in graphene. Chapter 3 contains the basic principles of THz time-domain spectroscopy, e.g., THz generation and detection methods, and polarization-resolved THz spectroscopy for the investigation of the magneto-optical responses of graphene. Chapter 4 describes our experimental details in a single pulse transmission experiment and a THz pump-THz probe experiment, including the description of the sample, intense THz pulse generation techniques and the data taking method for the pump-probe signals. Chapter 5 presents the experimental results observed in the single pulse transmission experiments and the THz pump-THz probe measurements. Ultrafast nonlinear magneto-optical responses of Landau-quantized graphene under the irradiation of intense off-resonant THz pulse are discussed. Chapter 6 provides the numerical simulations based on the density matrix formalism without using the rotating-wave approximation and we discuss the microscopic origin and mechanism of the nonlinear THz responses observed in our experiments. The feasibility for the detection of the higher harmonic generation from the non-equidistant LLs in graphene is also discussed. Finally, chapter 7 contains a brief summary of our findings and future prospects.

Chapter 2

Properties of graphene

Electrons in graphene behave like relativistic particles, i.e., massless Dirac fermions, due to the linear energy dispersion in the low-energy regime. Its unique electronic properties arising from the Dirac electron nature manifest themselves in carrier transports and various optical responses, and have attracted widespread interests. In this chapter, we first introduce the electronic properties of graphene without external electromagnetic fields and then review the intriguing electronic properties under a static magnetic field: the non-equidistant LLs. Finally, we review the peculiar optical properties of the LLs in graphene [19, 40].

2.1 Electronic properties of graphene

Graphene consists of carbon atoms with the honeycomb lattice structure, which is not a Bravais lattice and is constructed from two different sublattices called A and B sublattices as shown in Fig. 2.1 (a). The three vectors connecting a site on the A sublattice with nearest-neighbor sites on the B sublattice are given by

$$\boldsymbol{\delta}_1 = \frac{a}{2}\left(\mathbf{e}_x + \sqrt{3}\mathbf{e}_y\right), \quad \boldsymbol{\delta}_2 = \frac{a}{2}\left(\mathbf{e}_x - \sqrt{3}\mathbf{e}_y\right), \quad \boldsymbol{\delta}_3 = -a\mathbf{e}_x, \tag{2.1}$$

where $\mathbf{e}_x$ and $\mathbf{e}_y$ are the unit vectors in the x- and y-directions, respectively, and $a = 0.142$ nm is the distance between nearest-neighbor atoms [19, 40]. Because the Bravais lattice is spanned by the basis vectors of

$$\begin{aligned} \mathbf{a}_1 &= \frac{a}{2}\left(3\mathbf{e}_x + \sqrt{3}\mathbf{e}_y\right), \\ \mathbf{a}_2 &= \frac{a}{2}\left(3\mathbf{e}_x - \sqrt{3}\mathbf{e}_y\right), \end{aligned} \tag{2.2}$$

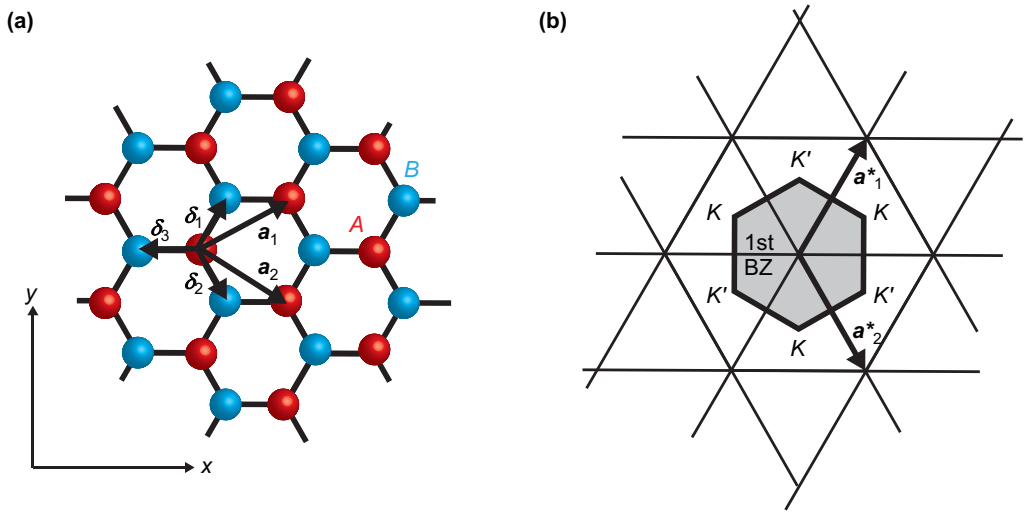

Figure 2.1: (a) Honeycomb lattice structure of carbon atoms. (b) First Brillouin zone in the momentum space.

the reciprocal lattice is spanned by the vectors of

$$\begin{aligned} \mathbf{a}_1^* &= \frac{2\pi}{3a}\left(\mathbf{e}_x + \sqrt{3}\mathbf{e}_y\right), \\ \mathbf{a}_2^* &= \frac{2\pi}{3a}\left(\mathbf{e}_x - \sqrt{3}\mathbf{e}_y\right). \end{aligned} \tag{2.3}$$

The first Brillouin zone (BZ) is shown as a shaded area in Fig. 2.1 (b), the six vertexes of which consist of two sets of inequivalent points of K and K', which cannot be connected with each other by the reciprocal lattice vectors.

Taking into account the electron hoppings to the nearest- and next-nearest-neighbor atoms, which are characterized by the nearest-neighbor hopping energy $t \sim 2.8$ eV and the next-nearest-neighbor hopping energy $t' \sim 0.1$ eV [41], respectively, we can obtain the energy dispersion of graphene within the tight-binding model as given by

$$\epsilon_\lambda(\boldsymbol{k}) = \lambda t\sqrt{3 + f(\boldsymbol{k})} - t' f(\boldsymbol{k}), \tag{2.4}$$

where λ represents $+$ for the upper band and $-$ for the lower band and

$$f(\boldsymbol{k}) = 2\cos\left(\sqrt{3}k_y a\right) + 4\cos\left(\frac{\sqrt{3}}{2}k_y a\right)\cos\left(\frac{3}{2}k_x a\right). \tag{2.5}$$

Because $t' \ll t$, we can neglect the second term on the right-hand side of Eq. (2.4) and $\epsilon_\lambda(\boldsymbol{k})$ becomes zero when $\boldsymbol{k} = \boldsymbol{K}$ and $\boldsymbol{k} = \boldsymbol{K}'$, where

$$\boldsymbol{K} = \frac{2\pi}{3a}\left(\mathbf{e}_x + \frac{1}{\sqrt{3}}\mathbf{e}_y\right), \quad \boldsymbol{K}' = \frac{2\pi}{3a}\left(\mathbf{e}_x - \frac{1}{\sqrt{3}}\mathbf{e}_y\right). \tag{2.6}$$

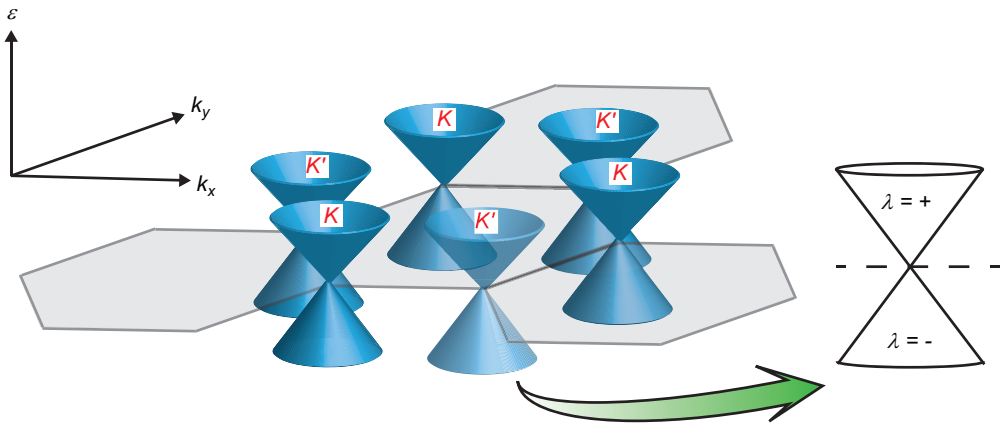

Figure 2.2: Schematic of linear energy dispersion around K and K' points.

This shows that the zero-energy points, named Dirac points, are located at K and K' points with the electron-hole symmetric energy dispersion of $\epsilon_\lambda(\boldsymbol{k}) = -\epsilon_{-\lambda}(\boldsymbol{k})$. In the low-energy regime close to the Dirac points, where $\boldsymbol{k} = \boldsymbol{K}(\boldsymbol{K}') + \boldsymbol{q}$ with $|\boldsymbol{q}| \ll |\boldsymbol{K}|$, the energy dispersion can be expanded to

$$\epsilon_\lambda(\boldsymbol{q}) \sim \lambda \hbar v_{\mathrm{F}} |\boldsymbol{q}| + O[(q/K)^2], \tag{2.7}$$

where $\boldsymbol{q}$ is the momentum measured from the Dirac points and the Fermi velocity v_{F} is given by $v_{\mathrm{F}} = 3ta/2\hbar \sim 1.02 \times 10^6$ m/s. In the low-energy excitation region, it is convenient to introduce the effective tight-binding Hamiltonian given by

$$H_K = \hbar v_{\mathrm{F}} \boldsymbol{\sigma} \cdot \boldsymbol{q} \tag{2.8}$$

and

$$H_{K'} = \hbar v_{\mathrm{F}} \boldsymbol{\sigma}^* \cdot \boldsymbol{q} \tag{2.9}$$

around K and K' points, respectively, where $\boldsymbol{\sigma} = (\sigma_x, \sigma_y)$ is the Pauli matrix vector with

$$\sigma_x = \begin{pmatrix} 0 & 1 \\ 1 & 0 \end{pmatrix}, \sigma_y = \begin{pmatrix} 0 & -i \\ i & 0 \end{pmatrix}. \tag{2.10}$$

Figure 2.2 shows the band structure of graphene, where the two bands linearly crosses at the K and K' points with a formation of the Dirac points, the apexes of the Dirac cones.

2.2 Landau quantization of Dirac electrons in graphene

The peculiar electronic properties originating from the relativistic nature also show up under the magnetic fields [19]. To investigate the electronic properties under the static

magnetic fields, we introduce the Peierls substitution

$$\boldsymbol{p} \to \boldsymbol{p} + e\boldsymbol{A}(\boldsymbol{r}), \tag{2.11}$$

where $\boldsymbol{p}$ is the electron momentum vector and $\boldsymbol{A}(\boldsymbol{r})$ is the vector potential related to the magnetic field through $\boldsymbol{B} = \boldsymbol{\nabla} \times \boldsymbol{A}(\boldsymbol{r})$. Then, we can obtain the Hamiltonian around K point in the presence of the magnetic field, which is given by

$$H_K = v_{\mathrm{F}} \boldsymbol{\sigma} \cdot (\boldsymbol{p} + e\boldsymbol{A}(\boldsymbol{r})) \,. \tag{2.12}$$

Here, we neglect the coupling between K and K' points, which allows us to treat each point separately, and omit the subscript of K hereinafter. To solve the eigenvalue problem of the Hamiltonian, it is convenient to introduce ladder operators

$$\begin{aligned} \hat{a} &= \frac{l_{\mathrm{B}}}{\sqrt{2}\hbar}(\pi_x - i\pi_y), \\ \hat{a}^\dagger &= \frac{l_{\mathrm{B}}}{\sqrt{2}\hbar}(\pi_x + i\pi_y), \end{aligned} \tag{2.13}$$

where $(\pi_x, \pi_y) = \boldsymbol{\pi} = \boldsymbol{p} + e\boldsymbol{A}(\boldsymbol{r})$ and the magnetic length l_{B} is described by

$$l_{\mathrm{B}} = \sqrt{\frac{\hbar}{eB}} \,. \tag{2.14}$$

Because π_x and π_y satisfy the commutation relation of

$$[\pi_x, \pi_y] = -i\frac{\hbar^2}{l_{\mathrm{B}}^2} \,, \tag{2.15}$$

the ladder operators $\hat{a}$ and $\hat{a}^\dagger$ fulfill the usual commutation relation

$$[\hat{a}, \hat{a}^\dagger] = 1 \,. \tag{2.16}$$

With Eqs. (2.12) and (2.13), the Hamiltonian under the magnetic field is rewritten by

$$H = \sqrt{2}\frac{\hbar v_{\mathrm{F}}}{l_{\mathrm{B}}} \begin{pmatrix} 0 & \hat{a} \\ \hat{a}^\dagger & 0 \end{pmatrix} \tag{2.17}$$

in terms of the ladder operators. Solving the eigenvalue equation

$$H \begin{pmatrix} u_n \\ v_n \end{pmatrix} = \epsilon_n \begin{pmatrix} u_n \\ v_n \end{pmatrix} , \tag{2.18}$$

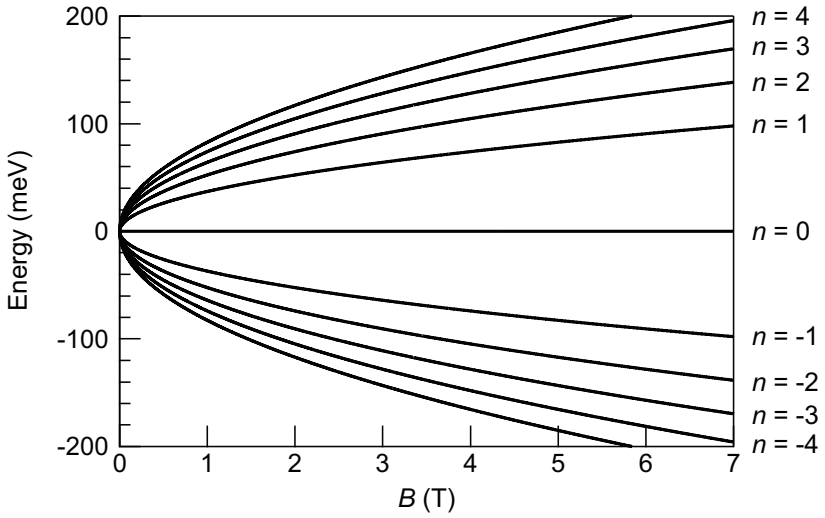

Figure 2.3: Non-equidistant LL energy spectrum of graphene.

we obtain the eigenenergy ϵ_n and eigenstate Ψ_n of the Hamiltonian as follows:

$$\epsilon_n = \mathrm{sgn}(n)\frac{\hbar v_{\mathrm{F}}}{l_{\mathrm{B}}}\sqrt{2n}, \tag{2.19}$$

$$\Psi_0 = \begin{pmatrix} 0 \\ |n=0\rangle \end{pmatrix}, \tag{2.20}$$

$$\text{and} \quad \Psi_{n\neq 0} = \frac{1}{\sqrt{2}}\begin{pmatrix} \mathrm{sgn}(n)||n|-1\rangle \\ |\,|n|\,\rangle \end{pmatrix}, \tag{2.21}$$

where the states of $||n|\rangle$ is the eigenstate of the number operator $\hat{a}^\dagger\hat{a}$ satisfying $\hat{a}^\dagger\hat{a}||n|\rangle = |n||n|\rangle$. As clearly seen in Eq. (2.19), the LL energy spectrum formed by Dirac electrons in graphene shows the peculiar properties; the $\sqrt{B}$- and $\sqrt{n}$-energy dependence and the existence of the zero-energy level. The non-equidistant LLs are depicted in Fig. 2.3, which is in sharp contrast to the usual equidistant LLs appearing in ordinary 2DEG.

Each LL has a large degeneracy, originating from the fact that the electron energy does not depend on the guiding-center position of the cyclotron motion. The guiding-center operator $\boldsymbol{R} = (X, Y)$ is defined by decomposing the position operator $\boldsymbol{r} = (x, y)$ through the relation

$$\boldsymbol{r} = \boldsymbol{R} + \boldsymbol{\eta}, \tag{2.22}$$

where $\boldsymbol{\eta} = (\eta_x, \eta_y)$ is the cyclotron variable describing the relative motion as shown in Fig. 2.4, which is given by $(\eta_x, \eta_y) = (\pi_y/eB, -\pi_x/eB)$. Because the guiding-center components X and Y satisfy the commutation relation

$$[X, Y] = -[\eta_x, \eta_y] = il_{\mathrm{B}}^2, \tag{2.23}$$

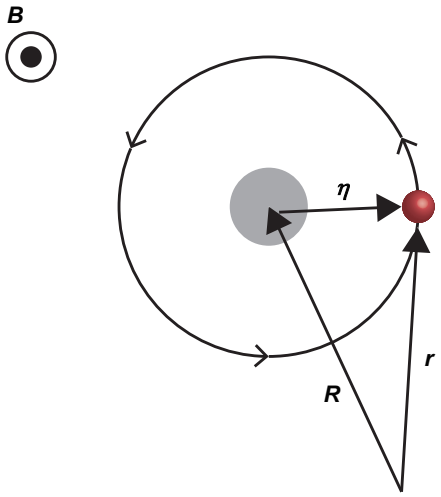

Figure 2.4: Schematic of the semi-classical cyclotron motion. The gray-shaded area represents the uncertainty of the guiding center.

we can define the ladder operators in the same manner as those in Eq. (2.13)

$$\begin{aligned} \hat{b} &= \frac{1}{\sqrt{2}l_{\mathrm{B}}}(X+iY), \\ \hat{b}^{\dagger} &= \frac{1}{\sqrt{2}l_{\mathrm{B}}}(X-iY), \end{aligned} \tag{2.24}$$

satisfying the commutation relation of $[\hat{b}, \hat{b}^{\dagger}] = 1$. Then, the eigenstates described by Eqs. (2.20) and (2.21) are rewritten into the complete quantum states by

$$\Psi_{n=0,m} = \begin{pmatrix} 0 \\ |n=0,m\rangle \end{pmatrix}, \tag{2.25}$$

$$\Psi_{n\neq 0,m} = \frac{1}{\sqrt{2}} \begin{pmatrix} \mathrm{sgn}(n)||n|-1,m\rangle \\ |\,|n|\,,m\rangle \end{pmatrix}, \tag{2.26}$$

where $m(\geq 0)$ and $|m\rangle$ are the eigenvalue and the eigenstate of the number operator $\hat{b}^{\dagger}\hat{b}$, respectively. Because the eigenenergy ϵ_n does not depend on m, the complete eigenstates including m show the large LL degeneracy. With the uncertainty area of the guiding-center position $\Delta X \Delta Y = 2\pi l_{\mathrm{B}}^2$ derived from the commutation relation of X and Y (shaded area in Fig. 2.4), the LL degeneracy N_{LL} is given by $4eB/h$, where the factor of 4 represents the two-fold spin and two-fold valley degeneracies.

2.3 Optical properties of the non-equidistant LLs in graphene

2.3.1 Optical transition selection rule

To study the optical responses of the LLs in graphene, we consider the light-matter interaction Hamiltonian with the help of the Peierls substitution introduced in the previous section [23, 42]. The light-matter interaction in Landau-quantized graphene is described by the total Hamiltonian

$$H = H_0 + H_{\rm int}, \tag{2.27}$$

where the non-interacting Hamiltonian H_0 and the light-matter interaction Hamiltonian $H_{\rm int}$ are given by

$$H_0 = v_{\rm F}\boldsymbol{\sigma}\cdot(\boldsymbol{p}+e\boldsymbol{A}_{\rm B}(\boldsymbol{r}))\,, \tag{2.28}$$

$$H_{\rm int} = ev_{\rm F}\boldsymbol{\sigma}\cdot\boldsymbol{A}_{\rm opt}(t), \tag{2.29}$$

where $\boldsymbol{A}_{\rm B}(\boldsymbol{r})$ generates the static magnetic field and $\boldsymbol{A}_{\rm opt}(t)$ describes the optical electric field with $\boldsymbol{E}(t) = -\frac{\partial}{\partial t}\boldsymbol{A}_{\rm opt}(t)$. Using the Fermi's golden rule, we can evaluate the optical transition rate from the n-th to m-th LL, W_{nm}, in the case of no LL broadenings as follows:

$$W_{nm} = \frac{2\pi}{\hbar}|\langle m|H_{\rm int}|n\rangle|^2\delta(\hbar\omega-(\epsilon_m-\epsilon_n)), \tag{2.30}$$

where $|n\rangle$ and ϵ_n are the eigenstate and the eigenenergy of H_0. When we choose the Landau gauge such as $\boldsymbol{A}_{\rm B}(\boldsymbol{r}) = (0, Bx)$, the eigenstate can be described as follows [43]:

$$\Psi_{n,k_y}(\boldsymbol{r}) = \frac{C_n}{\sqrt{L}}\exp(-ik_y y)\begin{pmatrix}\mathrm{sgn}(n)i^{|n|-1}\phi_{|n|-1}\\ i^{|n|}\phi_{|n|}\end{pmatrix} \tag{2.31}$$

with

$$C_n = \begin{cases}1 & (n=0)\\ \dfrac{1}{\sqrt{2}} & (n\neq 0)\end{cases} \tag{2.32}$$

and

$$\phi_{|n|} = \frac{1}{\sqrt{2^{|n|}|n|!\sqrt{\pi}l_{\rm B}}}\exp\left[-\frac{1}{2}\left(\frac{x-l_{\rm B}^2k_y}{l_{\rm B}}\right)^2\right]H_{|n|}\left(\frac{x-l_{\rm B}^2k_y}{l_{\rm B}}\right), \tag{2.33}$$

where L^2 is the area of the system and $H_n(x)$ is the Hermite polynomial. If we define the left- and right-handed circular polarization vectors as $\hat{e}_{\rm L} = (\hat{x}-i\hat{y})/\sqrt{2}$ and $\hat{e}_{\rm R} =$

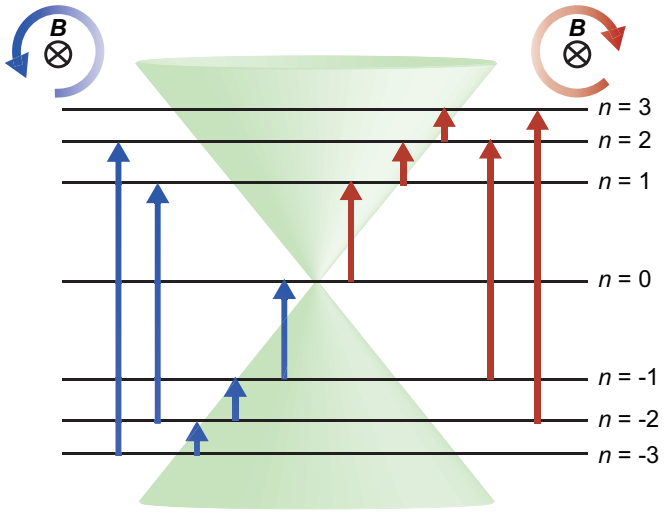

Figure 2.5: Optical transition selection rule of the non-equidistant LL transitions in graphene.

$(\hat{x} + i\hat{y})/\sqrt{2}$, respectively, the optical matrix element appearing in Eq. (2.30) is written by

$$\langle m|H_{\rm int}|n\rangle = \sqrt{2}ev_{\rm F}C_mC_n(-1)^{|m|-1}i^{|m|+|n|-1} \times(\mathrm{sgn}(m)\delta_{|m|-1,|n|}\hat{e}_{\rm L} - \mathrm{sgn}(n)\delta_{|m|,|n|-1}\hat{e}_{\rm R})\cdot\boldsymbol{A}_{\rm opt}(t) \tag{2.34}$$

with using the expression of the eigenstate in Eq. (2.31). Because Eq. (2.34) takes a finite value when $|m| = |n| \pm 1$, this equation shows the optical transition selection rule of the LLs in graphene

$$\Delta|n| = \pm 1, \tag{2.35}$$

which has been experimentally confirmed in the far-infrared transmission experiment [22]. Furthermore, considering the relations of the inner product, $\hat{e}_{\rm L(R)}\cdot\hat{e}^*_{\rm L(R)} = 1$ and $\hat{e}_{\rm L(R)}\cdot\hat{e}^*_{\rm R(L)} = 0$, we find that the absorption of left-handed circularly polarized light occurs for the $n(<0)$-th to the $\pm(|n|-1)$-th LL transitions and that of right-handed circularly polarized light is allowed for the n-th to the $(|n|+1)$-th LL transitions. This unique optical transition selection rule is illustrated in Fig. 2.5.

2.3.2 Giant dipole moment matrix elements between LLs

Next, we derive the expression of the dipole moment matrix elements of the LL transitions in graphene. The dipole moment matrix is defined as $\boldsymbol{\mu} = e\hat{\boldsymbol{r}}$, where $\hat{\boldsymbol{r}}$ is the position operator. First, we evaluate the following commutator

$$[\hat{\boldsymbol{r}}, H_0] = [\hat{\boldsymbol{r}}, v_{\rm F}\boldsymbol{\sigma}\cdot\hat{p}] + [\hat{\boldsymbol{r}}, v_{\rm F}\boldsymbol{\sigma}\cdot\boldsymbol{A}_{\rm B}(\boldsymbol{r})]\ . \tag{2.36}$$

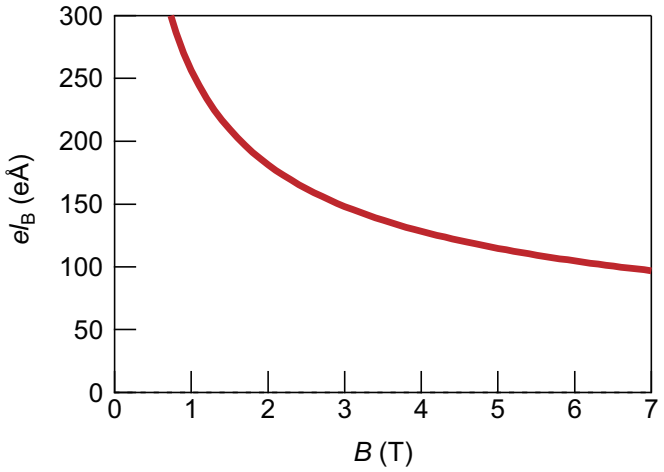

Figure 2.6: Magnetic field dependence of the typical magnitude of the transition dipole moments between LLs, el_{B}.

Because the second term on the right-hand side is zero due to the fact that $\boldsymbol{A}_{\mathrm{B}}$ is a function of $\boldsymbol{r}$, Eq. (2.36) becomes

$$[\hat{\boldsymbol{r}}, H_0] = v_{\mathrm{F}}\boldsymbol{\sigma} \cdot [\hat{\boldsymbol{r}}, \hat{p}] = i\hbar v_{\mathrm{F}}\boldsymbol{\sigma}. \tag{2.37}$$

Because the matrix element of the commutator on the left side of Eq. (2.36) is described by

$$\langle m|[\hat{\boldsymbol{r}}, H_0]|n\rangle = \langle m|\hat{\boldsymbol{r}}H_0|n\rangle + \langle m|H_0\hat{\boldsymbol{r}}|n\rangle = (\epsilon_n - \epsilon_m)\langle m|\hat{\boldsymbol{r}}|n\rangle \tag{2.38}$$

in the basis of the eigenstates of H_0, by combining Eqs. (2.37) and (2.38), the dipole moment matrix elements are written by

$$\boldsymbol{\mu}_{mn} = e\langle m|\hat{\boldsymbol{r}}|n\rangle = \frac{i\hbar e}{\epsilon_n - \epsilon_m}\langle m|v_{\mathrm{F}}\boldsymbol{\sigma}|n\rangle\ . \tag{2.39}$$

Substituting the expression of the eigenstate described by Eq. (2.31) into Eq. (2.39), we finally obtain the analytic expression for the dipole moment matrix elements as follows [42]:

$$\begin{aligned}\boldsymbol{\mu}_{mn} \quad = \quad & \frac{i\hbar e v_{\mathrm{F}} C_m C_n (-1)^{|m|-1} i^{|m|+|n|-1}}{\epsilon_n - \epsilon_m} \\ & \times(\mathrm{sgn}(m)\delta_{|m|-1,|n|}(\hat{x} - i\hat{y}) - \mathrm{sgn}(n)\delta_{|m|,|n|-1}(\hat{x} + i\hat{y})).\end{aligned} \tag{2.40}$$

Because the magnitude of the transition dipole moments between the LLs is on the order of el_{B} as shown by

$$|\boldsymbol{\mu}_{mn}| \sim \frac{e\hbar v_{\mathrm{F}}}{\epsilon_n - \epsilon_m} = \frac{el_{\mathrm{B}}}{\sqrt{2}(\mathrm{sgn}(n)\sqrt{n} - \mathrm{sgn}(m)\sqrt{m})} \propto el_{\mathrm{B}}, \tag{2.41}$$

the dipole moments become very large in Landau-quantized graphene (Fig. 2.6). We also note that the dipole moment matrix elements are nonzero when $|m| = |n| \pm 1$, which also exhibits the optical transition selection rule explained in Eq. (2.35).

Chapter 3

Principles of polarization-resolved THz spectroscopy

3.1 Terahertz time-domain spectroscopy (THz-TDS)

The THz frequency region (1 THz $\sim$ 4.14 meV) is located in a very intriguing frequency range both from the aspect of application like the THz imaging [44] and from fundamental physics research. In condensed matter physics, the THz range attracts many interests because it enables direct access to intraband responses and covers fascinating energy scales such as the exciton binding energy in semiconductors, the BCS gap energy in superconductors, and the LL energy spacing in 2DEG.

Recent development of the broadband laser sources have enabled the generation and detection of coherent THz pulses and opened up new spectroscopic techniques. Here, we introduce the so-called terahertz time-domain spectroscopy (THz-TDS) based on femtosecond pulse laser sources. Unlike the far-infrared interferometric techniques like FTIR (Fourier transform infrared spectroscopy), the THz-TDS directly detects the waveform of the THz electric field in the time domain. The direct access to the electric field leads to the simultaneous determination of the amplitude and phase of the field component in the frequency domain, which allows us to detect the complex response function of samples without Kramers-Kronig transform. In this section, we describe the basic principles of the THz-TDS: the THz generation and detection with electro-optic crystals, which have been intensively studied [45–48] and are commonly used.

3.1.1 THz generation

Several methods for THz pulse generation have been developed with a variety of sources such as photoconductive antenna on semiconductors, electro-optic crystals, and air-plasma induced by strong ultrafast laser pulses. Here, we describe the mechanism of THz generation from commonly used (110) zinc-blende electro-optic crystals such as ZnTe

and GaP [48, 49]. Compared to the photoconductive antenna, the THz electric field emitted from the electro-optic crystals can contain high-frequency components indispensable to the study of LLs in graphene. Unlike the plasma method, the THz pulse can be easily generated even by a weak optical pulse.

Because of the lack of the inversion symmetry, the (110) zinc-blende electro-optic crystals possess the second-order nonlinear response to a driving optical pulse. Optical rectification, one of the second-order nonlinear processes, generates low-frequency electric field in the THz frequency corresponding to the frequency difference within spectral components of a single optical pulse. For this method, a ZnTe crystal is very useful since the phase-matching condition is well satisfied for the optical pulse with the 800-nm wavelength from Ti:sapphire-based femtosecond laser sources. A GaP crystal is another representative electro-optic crystal for the broadband THz pulse generation up to 7 THz owing to the high-frequency phonon modes compared to ZnTe.

To view the THz generation process by the optical rectification, we introduce the second-order polarization in the time domain $\tilde{P}_i^{(2)}(t)$ as follows:

$$\tilde{P}_i^{(2)}(t) = \epsilon_0 \int_0^\infty d\tau_1 \int_0^\infty d\tau_2 \sum_{jk} R_{ijk}^{(2)}(\tau_1, \tau_2) E_j(t-\tau_1) E_k(t-\tau_2), \tag{3.1}$$

where the indices i, j, k represent the Cartesian components, $R_{ijk}^{(2)}$ is the second-order response function satisfying the causality condition that $R_{ijk}^{(2)}(\tau_1, \tau_2) = 0$ if $\tau_1 < 0$ or $\tau_2 < 0$, ϵ_0 is the permittivity of free space, and $E_i(t)$ is the i-component of the applied electric field. Equation (3.1) can be rewritten with Fourier components of the electric field by

$$\begin{aligned} \tilde{P}_i^{(2)}(t) &= \epsilon_0 \int_{-\infty}^\infty \frac{d\omega_1}{2\pi} \int_{-\infty}^\infty \frac{d\omega_2}{2\pi} \sum_{jk} \chi_{ijk}^{(2)}(\omega_1+\omega_2; \omega_1, \omega_2) \\ &\times E_j(\omega_1) E_k(\omega_2) \mathrm{e}^{-i(\omega_1+\omega_2)t}, \end{aligned} \tag{3.2}$$

with

$$\chi_{ijk}^{(2)}(\omega_1+\omega_2; \omega_1, \omega_2) = \int_0^\infty d\tau_1 \int_0^\infty d\tau_2 R_{ijk}^{(2)}(\tau_1, \tau_2) \mathrm{e}^{i(\omega_1\tau_1+\omega_2\tau_2)}, \tag{3.3}$$

where $\chi_{ijk}^{(2)}$ is the second-order susceptibility and $\boldsymbol{E}(-\omega) = \boldsymbol{E}^*(\omega)$. Because the electric field emitted by the second-order polarization is given by

$$\mathbf{E}(t) \propto \frac{\partial^2}{\partial t^2} \mathbf{P}^{(2)}(t), \tag{3.4}$$

the frequency of the emitted electric field is $\omega_1 + \omega_2$. When an ultrashort optical pulse, which contains broad spectral components, is used to irradiate the zinc-blende electro-optic crystals, frequency mixing between ω_1 and $-\omega_2$ included in the optical pulse generates an $\omega_1 - \omega_2$ frequency electric field from the crystals via the second-order nonlinear process, which corresponds to electric field in the THz frequency range.

3.1.2 THz detection

Linear electro-optic effect: Pockels effect

The refractive index of the zinc-blende electro-optic materials can be changed under the electric field through the first-order electro-optic effect, which is referred to as the Pockels effect. The THz electric field can be detected by using the refractive index change for ultrafast optical pulses. Because the Pockels effect can be regarded as the reverse process of the optical rectification, the THz detection mechanism can be explained in terms of the second-order nonlinear process by a complete frequency-domain description [50]. However, for its simplicity, here we introduce an alternative approach with the notion of the index ellipsoid to describe the Pockels effect and the THz detection technique [48,49].

In the case of a (110) zinc-blende electro-optic crystal under the THz electric field irradiation perpendicular to the $[110]$ axis of the crystal, the index ellipsoid is described in (x, y, z) coordinate system, shown in Fig. 3.1, by

$$\frac{x^2+y^2+z^2}{n_0^2} + 2r_{41}E_x^{\mathrm{THz}}yz + 2r_{41}E_y^{\mathrm{THz}}zx + 2r_{41}E_z^{\mathrm{THz}}xy = 1, \tag{3.5}$$

where n_0 is the refractive index of the zinc-blende crystal, r_{41} is the electro-optic coefficient of the crystal and E_i^{THz} is the i-component of the applied THz electric field. Rewriting Eq. (3.5) in $(x', y', z' = z)$ coordinate system (Fig. 3.1) and setting $x' = 0$, we obtain the equation of the index ellipse on the (110) plane

$$\left(\frac{1}{n_0^2} - r_{41}E^{\mathrm{THz}}\cos\phi\right)y'^2 + \frac{z'^2}{n_0^2} + \left(2r_{41}E^{\mathrm{THz}}\sin\phi\right)y'z' = 1. \tag{3.6}$$

Transformation of Eq. (3.6) to (y'', z'') coordinate system (Fig. 3.1) gives the equation

$$\begin{aligned}\left[\frac{1}{n_0^2} + \frac{1}{2}r_{41}E^{\mathrm{THz}}\left(-\cos\phi + \sqrt{1+3\sin^2\phi}\right)\right]y"^2 \quad + \\ \left[\frac{1}{n_0^2} + \frac{1}{2}r_{41}E^{\mathrm{THz}}\left(-\cos\phi - \sqrt{1+3\sin^2\phi}\right)\right] \quad z"^2 \quad = 1.\end{aligned} \tag{3.7}$$

From Eq. (3.7), we obtain the refractive indices in y''- and z''- directions as follows:

$$\begin{aligned}\frac{1}{n_{y''}^2} &= \left[\frac{1}{n_0^2} + \frac{1}{2}r_{41}E^{\mathrm{THz}}\left(-\cos\phi + \sqrt{1+3\sin^2\phi}\right)\right] \\ \Rightarrow n_{y"} &\approx n_0 + \frac{n_0^3 r_{41}E^{\mathrm{THz}}}{4}\left(\cos\phi - \sqrt{1+3\sin^2\phi}\right)\end{aligned} \tag{3.8}$$

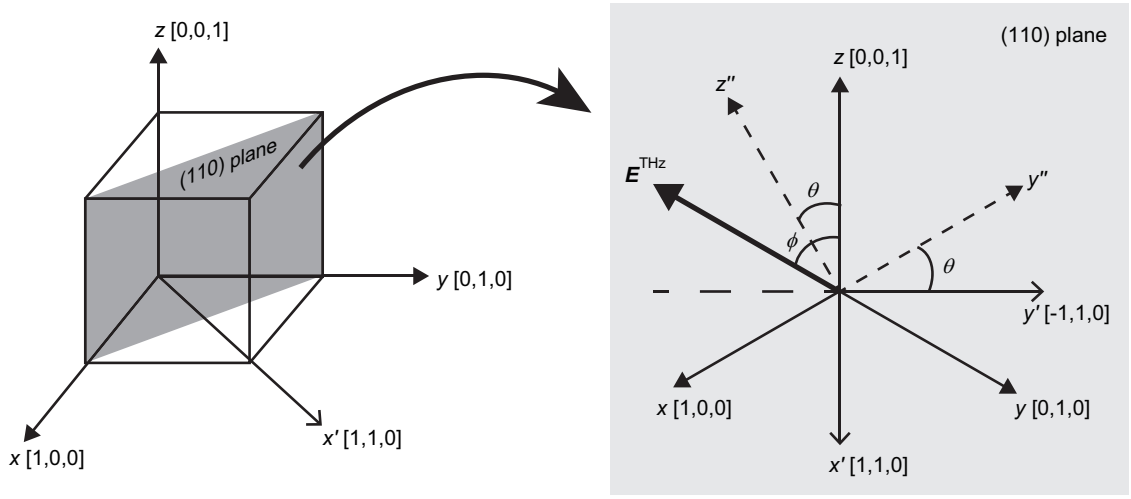

Figure 3.1: Definition of coordinate systems and the angles θ and ϕ on the (110) plane of the zinc-blende electro-optic crystal.

and

$$\begin{aligned} \frac{1}{n_{z''}^2} &= \left[\frac{1}{n_0^2} + \frac{1}{2} r_{41} E^{\mathrm{THz}} \left(-\cos\phi - \sqrt{1+3\sin^2\phi}\right)\right] \\ \Rightarrow n_{z''} &\approx n_0 + \frac{n_0^3 r_{41} E^{\mathrm{THz}}}{4}\left(\cos\phi + \sqrt{1+3\sin^2\phi}\right). \end{aligned} \tag{3.9}$$

Finally, we can find that the refractive index difference between the indices in y''- and z''-directions is proportional to the amplitude of the applied THz electric field and is given by

$$\Delta n \equiv (n_{z''} - n_{y''}) = \frac{n_0^3 r_{41} E^{\mathrm{THz}} \sqrt{1+3\sin^2\phi}}{2}. \tag{3.10}$$

Electro-optic sampling with balanced detection technique

As given in Eq. (3.10), the sign and the amplitude of the THz electric field are related to the refractive index difference and therefore can be measured by the electro-optic sampling technique with an ultrashort near-infrared pulse, which we call a gate pulse. As schematically shown in Fig. 3.2, the gate pulse linearly polarized along the y'-direction experiences the phase difference Γ between y''- and z''-components of the gate pulse induced by the THz electric field during propagation in the electro-optic crystal with the thickness d. The phase difference Γ is given by $\Gamma = (2\pi d/\lambda)\Delta n$, where λ is the central wavelength of the gate pulse. Because of the phase difference, the gate pulse is elliptically polarized after passing through the crystal.

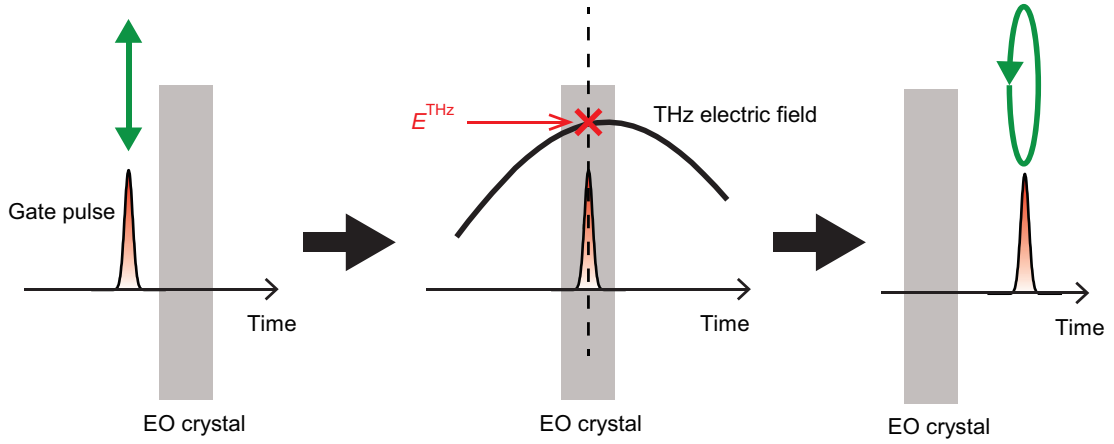

Figure 3.2: Schematic of electro-optic sampling method. Green arrows indicate the polarization states of the gate pulse before and after the electro-optic (EO) crystal.

As a method to measure the phase difference Γ, here we explain the balanced detection technique as shown in Fig. 3.3. A gate pulse linearly polarized in the y'-direction obtains the phase difference from an (110) zinc-blende electro-optic crystal. After passing through the crystal, the gate pulse propagates through a $\lambda/4$ plate which creates the phase shift between the fast and the slow axes by $\pi/2$. After the $\lambda/4$ plate, it is divided into y'- and z-components by a Wollaston prism. The intensity difference ΔI of the two components is measured by a balanced photo-detector. Without the THz electric field, the $\lambda/4$ plate makes the intensities balanced and $\Delta I = 0$. Under the THz irradiation, the intensity difference between the two beams becomes nonzero and it is proportional to the amplitude of the THz electric field.

To take a further look at the principle of the balanced detection, we introduce Jones matrix formalism. For simplicity, we define that the incident gate pulse is linearly polarized in the y'-direction, described by

$$\boldsymbol{E}_{\mathrm{in}} = \begin{pmatrix} E \\ 0 \end{pmatrix}. \tag{3.11}$$

The Jones matrices of the zinc-blende crystal and $\lambda/4$ plate are described by

$$\boldsymbol{J}_{\mathrm{xtal}} = \begin{pmatrix} \cos\theta & -\sin\theta \\ \sin\theta & \cos\theta \end{pmatrix} \begin{pmatrix} \mathrm{e}^{i\gamma_{y''}} & 0 \\ 0 & \mathrm{e}^{i\gamma_{z''}} \end{pmatrix} \begin{pmatrix} \cos\theta & \sin\theta \\ -\sin\theta & \cos\theta \end{pmatrix} \tag{3.12}$$

and

$$\boldsymbol{J}_{\lambda/4} = \begin{pmatrix} \cos\frac{\pi}{4} & -\sin\frac{\pi}{4} \\ \sin\frac{\pi}{4} & \cos\frac{\pi}{4} \end{pmatrix} \begin{pmatrix} \mathrm{e}^{-i\frac{\pi}{4}} & 0 \\ 0 & \mathrm{e}^{i\frac{\pi}{4}} \end{pmatrix} \begin{pmatrix} \cos\frac{\pi}{4} & \sin\frac{\pi}{4} \\ -\sin\frac{\pi}{4} & \cos\frac{\pi}{4} \end{pmatrix}, \tag{3.13}$$

respectively, where

$$\gamma_{y''} \equiv (2\pi d/\lambda) n_{y''}, \gamma_{z''} \equiv (2\pi d/\lambda) n_{z''}. \tag{3.14}$$

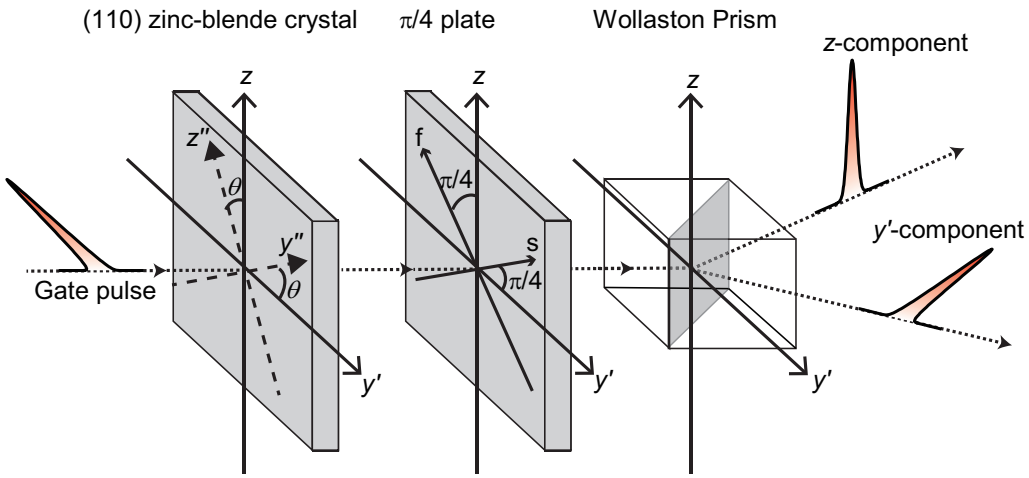

Figure 3.3: Schematic of the balanced electro-optic detection. The letters f and s depicted in the $\lambda/4$ plate represent fast and slow axes, respectively.

We obtain the intensity difference between the detected y'- and z-components of the gate pulse through the relation of $\boldsymbol{E}_{\rm tr} = \boldsymbol{J}_{\lambda/4}\boldsymbol{J}_{\rm xtal}\boldsymbol{E}_{\rm in}$, where $\boldsymbol{E}_{\rm tr}$ is the electric field before the Wollaston prism. The intensity difference is given by

$$\begin{aligned}\Delta I &= |E|^2 \sin\Gamma \sin 2\theta \\ &\approx |E|^2 \Gamma \sin 2\theta = |E|^2 \frac{\pi d n_0^3 r_{41} E^{\rm THz}\sqrt{1+3\sin^2\phi}}{\lambda}\sin 2\theta, \end{aligned} \tag{3.15}$$

where ϕ is the angle between THz electric field and z axis defined in Fig. 3.1. Especially, when we set $\phi = \pi/2$ and $\theta = \pi/4$, the THz electric field can be written by

$$E^{\rm THz} = \frac{\Delta I}{I}\frac{\lambda}{2\pi d n_0^3 r_{41}}, \tag{3.16}$$

which clearly shows that the THz electric field is detected by measuring ΔI.

3.1.3 Experimental setup for THz-TDS

To explain the details of THz-TDS, we show the typical experimental setup in Fig. 3.4. The output pulse of the femtosecond laser system is divided into two beams by a beam splitter (BS), one of which is used for the gate pulse of the THz detection and the other is for the THz generation. The gate pulse is reflected by a pair of mirrors mounted on a mechanical delay stage (DS) to vary the delay time of the gate pulse to the THz pulse, which we call the gate delay time $t_{\rm gate}$. After the reflection from the mirrors on the DS, the gate pulse passes through a linear polarizer, which sets the polarization of the incoming

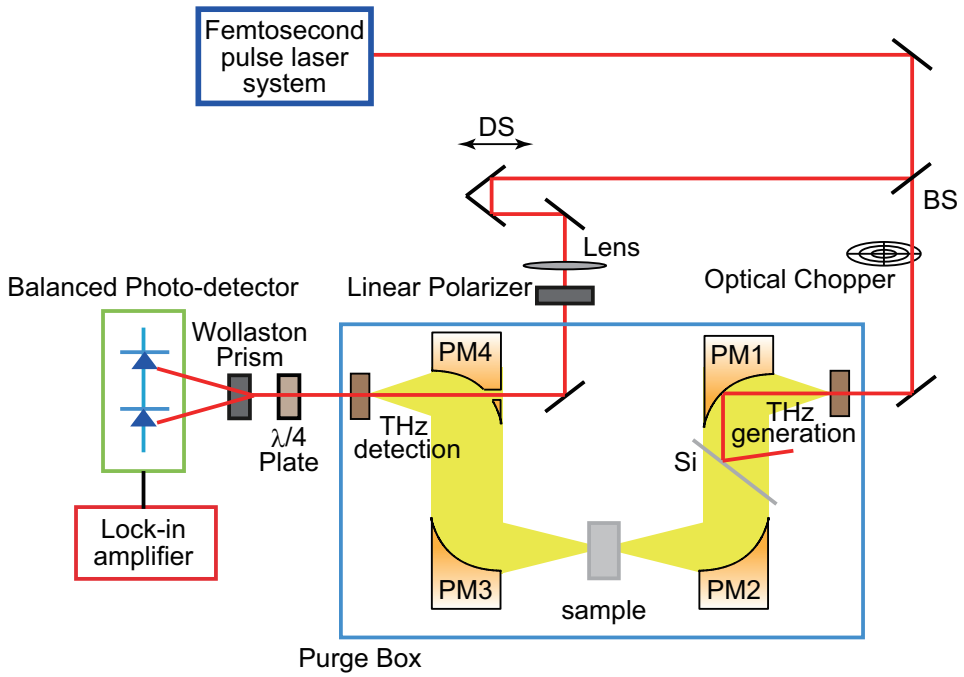

Figure 3.4: Experimental setup for THz-TDS. BS, DS and PM denote beam splitter, delay stage, and parabolic mirror, respectively.

gate pulse linear, and is used to irradiate an electro-optic crystal for the electro-optic sampling. The THz electric field waveform is obtained by changing the gate delay time and detecting the THz electric fields at every point in the THz pulse as shown in Fig. 3.5.

Another beam divided from the output of the laser system for the THz generation is modulated by an optical chopper before the irradiation onto the electro-optic crystal in order to perform the lock-in detection. The femtosecond optical pulse transmitted through the THz generation crystal is blocked by a high-resistivity Si wafer which transmits the generated THz pulse without absorption. The amplitude of the THz electric field is reduced to $\sim 70\%$ after the Si wafer due to the Fresnel reflection loss of the wafer. The generated THz beam is collimated by the parabolic mirror 1 (PM1) and focused onto a sample by the PM2. After the sample, the THz beam is again collimated and focused onto the electro-optic crystal for the THz detection. The electric signal detected by the balanced photo-detector is sent to a lock-in amplifier with a reference signal from the optical chopper. The space where the THz pulse propagates is purged by dry air, as indicated by a Purge Box in Fig. 3.4, in order to avoid water vapor absorption of the THz radiation.

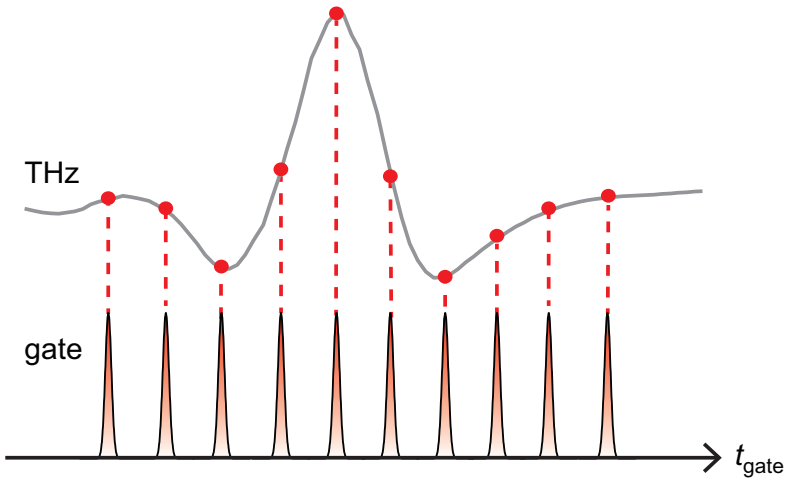

Figure 3.5: Schematic of the measurement of a THz electric field waveform by changing the gate delay time t_{gate}.

3.2 THz magneto-optical spectroscopy

3.2.1 Faraday rotation and description of polarization state

As the incident light linearly polarized in the x-direction propagates in the z-direction through a material under a magnetic field applied in the direction of the light propagation, the polarization axis rotates from the incident one and also becomes elliptical, which is known as the Faraday effect (Fig. 3.6). This phenomenon originates from the difference between complex refractive indices for the right- and left-handed circularly polarized light, which is induced by the violation of time-reversal symmetry due to the applied magnetic field.

In general, the polarization state of the light can be described by using rotation angle θ and ellipticity η [51]. If we define $R(\omega) = E_y(\omega)/E_x(\omega) = [E_y^0(\omega)/E_x^0(\omega)]e^{i\delta}$, where $E_{x(y)}(\omega) = E_{x(y)}^0(\omega)e^{i\delta_{x(y)}}$ is the Fourier component of the $x(y)$-component of the elliptically polarized electric field $E_{x(y)}(t)$ and $\delta = \delta_y - \delta_x$, the rotation angle θ and the ellipticity η can be described by using $R(\omega)$ as follows:

$$\begin{cases} \theta(\omega) = \frac{1}{2}\tan^{-1}\dfrac{2\mathrm{Re}R(\omega)}{1-|R(\omega)|^2} \\ \eta(\omega) = \tan\left[\frac{1}{2}\sin^{-1}\dfrac{2\mathrm{Im}R(\omega)}{1+|R(\omega)|^2}\right]. \end{cases} \tag{3.17}$$

The ellipticity η is related to the half-lengths of the major and minor axes of the ellipse, a and b, respectively, through the relation of $\eta = \tan^{-1}(\pm b/a)$ (Fig. 3.7). The sign of η

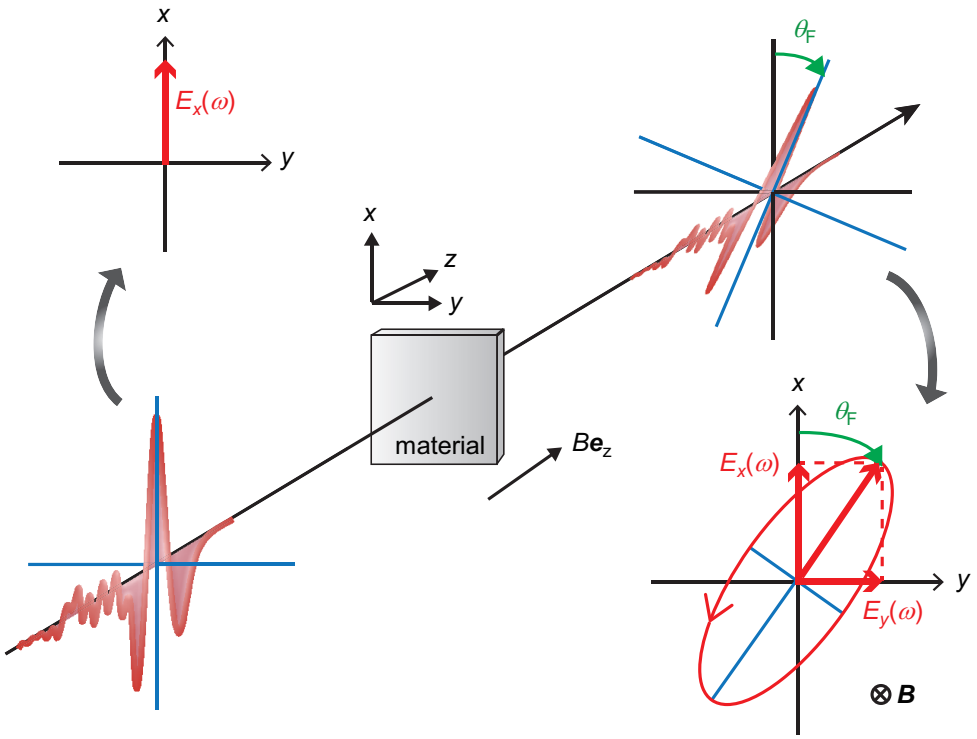

Figure 3.6: Schematic of Faraday effect. θ_{F} represents the Faraday rotation angle.

corresponds to $+$ for $\sin\delta > 0$ and $-$ for $\sin\delta < 0$. In the small rotation angle limit, Eq. (3.17) is rewritten by

$$\begin{cases} \theta(\omega) \approx \mathrm{Re}R(\omega) \\ \eta(\omega) \approx \mathrm{Im}R(\omega). \end{cases} \tag{3.18}$$

3.2.2 Faraday rotation in graphene

Next, we consider the relation between the Faraday rotation and the optical conductivity for the case of graphene [52]. From the Maxwell's equations, the wave equation describing the propagation of electromagnetic waves reads

$$\frac{\partial^2 \boldsymbol{E}}{\partial z^2} = \frac{\omega^2 \epsilon}{c^2}\boldsymbol{E} - \omega\mu_0 \boldsymbol{j}\delta(z), \tag{3.19}$$

where c is the speed of light, ϵ is the dielectric constant, μ_0 is the vacuum permeability, and $\boldsymbol{j}$ is the surface current density vector. We assume that graphene is surrounded by

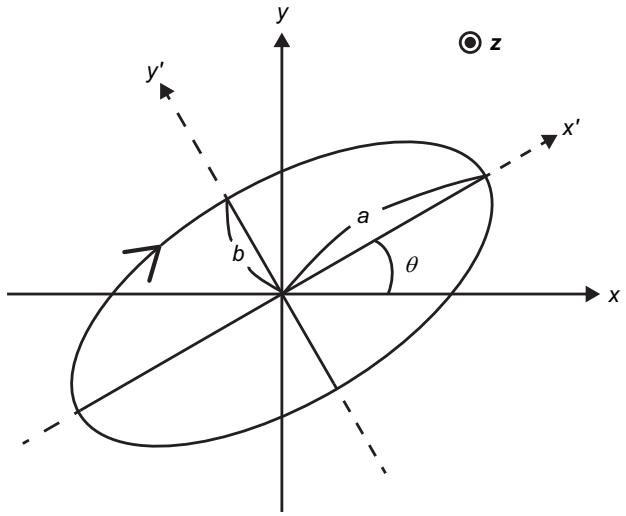

Figure 3.7: Polarization state of the elliptically polarized light. a and b represent the half-lengths of the major and minor axes of the ellipse, respectively, and θ is the rotation angle.

two lossless dielectric materials with the dielectric constants of ϵ_1 and ϵ_0 and located at the position of $z = 0$ as shown in Fig. 3.8. The electric field propagates in the direction of z. The incident, reflected and transmitted electric fields, denoted by $\boldsymbol{E}^{\rm i}$, $\boldsymbol{E}^{\rm r}$ and $\boldsymbol{E}^{\rm t}$, respectively, are described by

$$\begin{aligned} \boldsymbol{E}^{\rm i} &= \boldsymbol{E}^{\rm i}_0 \exp(i\omega t - iq_0 z) \qquad (z < 0) \\ \boldsymbol{E}^{\rm r} &= \boldsymbol{E}^{\rm i}_0 \exp(i\omega t + iq_0 z) \qquad (z < 0) \\ \boldsymbol{E}^{\rm t} &= \boldsymbol{E}^{\rm i}_0 \exp(i\omega t - iq_1 z) \qquad (z > 0), \end{aligned} \tag{3.20}$$

where $q_{0,1} = n_{0,1}\omega/c$ with the refractive index of $n_{0,1} = \sqrt{\epsilon_{0,1}}$. By integrating Eq. (3.19) from $z = 0^-$ to $z = 0^+$, we obtain a boundary condition at $z = 0$ given by

$$-iq_1 \boldsymbol{E}^{\rm t} + iq_0(\boldsymbol{E}^{\rm i} - \boldsymbol{E}^{\rm r}) = \omega\mu_0 \boldsymbol{j}. \tag{3.21}$$

In addition to this boundary condition, the tangential component of the electric fields must be continuous, written by

$$\boldsymbol{E}^{\rm t} = \boldsymbol{E}^{\rm i} + \boldsymbol{E}^{\rm r}. \tag{3.22}$$

If we introduce circularly polarized coordinates and define $E_\pm = E_x \mp iE_y$ and $j_\pm = j_x \mp ij_y$, we can obtain the equation relating the incident and transmitted electric fields, satisfying the relation

$$E^{\rm t}_\pm(\omega) = \frac{2n_0}{n_1 + n_0} \times E^{\rm i}_\pm(\omega) - \frac{Z_0}{n_1 + n_0} \times j_\pm(\omega), \tag{3.23}$$

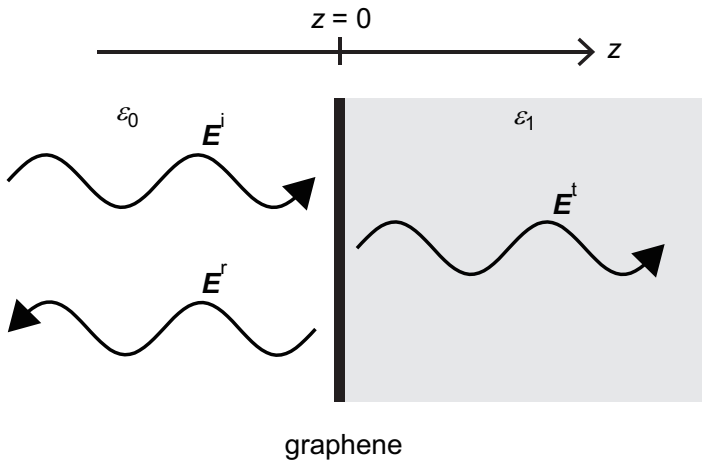

Figure 3.8: Configuration of graphene and dielectric materials with the dielectric constants of ϵ_1 (the right-hand side of graphene: gray-shaded area) and ϵ_0 (the left-hand side of graphene).

where Z_0 is the vacuum impedance.

By using the optical conductivities of graphene, the surface current density can be described by

$$\begin{pmatrix} j_x(\omega) \\ j_y(\omega) \end{pmatrix} = \begin{pmatrix} \sigma_{xx}(\omega) & \sigma_{xy}(\omega) \\ \sigma_{yx}(\omega) & \sigma_{yy}(\omega) \end{pmatrix} \begin{pmatrix} E_x(\omega) \\ E_y(\omega) \end{pmatrix}, \tag{3.24}$$

where $\sigma_{xx}(\omega)$ and $\sigma_{yy}(\omega)$ are the optical longitudinal conductivities and $\sigma_{xy}(\omega)$ and $\sigma_{yx}(\omega)$ are the optical Hall conductivities. In graphene, $\sigma_{yy}(\omega) = \sigma_{xx}(\omega)$ and $\sigma_{yx}(\omega) = -\sigma_{xy}(\omega)$ due to the isotropy of the system. When we define $\sigma_{\pm}(\omega) = \sigma_{xx}(\omega) \pm i\sigma_{xy}(\omega)$, we can write the surface current density in the circularly polarized coordinates as

$$j_{\pm}(\omega) = \sigma_{\pm}(\omega) E_{\pm}(\omega). \tag{3.25}$$

Substituting Eq. (3.25) into Eq. (3.23), we obtain $E^{\mathrm{t}}_{\pm}(\omega)/E^{\mathrm{i}}_{\pm}(\omega) \equiv t_{\pm} = 2n_0/(n_0 + n_1 + Z_0\sigma_{\pm}(\omega))$. Rewriting Eq. (3.17) with $E_{\pm}$, we obtain the expression for the Faraday rotation angle $\theta_{\mathrm{F}}(\omega)$ and the ellipticity $\eta_{\mathrm{F}}(\omega)$ in the case of graphene with optical conductivities given by

$$\begin{cases} \theta_{\mathrm{F}}(\omega) = -\dfrac{1}{2}\arg\left(\dfrac{t_+}{t_-}\right) \\ \eta_{\mathrm{F}}(\omega) = \dfrac{|t_+| - |t_-|}{|t_-| + |t_+|}. \end{cases} \tag{3.26}$$

Especially, when $1 >> Z_0\sigma_{\pm}/(n_0+n_1)$, Eq. (3.26) can be expressed by

$$\begin{cases} \theta_{\mathrm{F}}(\omega) \approx \dfrac{Z_0}{n_0+n_1}\mathrm{Re}\sigma_{xy}(\omega) \\ \eta_{\mathrm{F}}(\omega) \approx \dfrac{Z_0}{n_0+n_1}\mathrm{Im}\sigma_{xy}(\omega). \end{cases} \tag{3.27}$$

Equation (3.27) shows that the Faraday rotation angle and the ellipticity are proportional to the real and imaginary parts of the optical Hall conductivity of graphene, respectively.

3.2.3 Polarization detection technique

As shown in Eq. (3.17), we have to measure the electric field waveforms of x- and y-components of the transmitted THz electric field, $E_x^{\mathrm{t}}(t)$ and $E_y^{\mathrm{t}}(t)$, respectively, to eval-

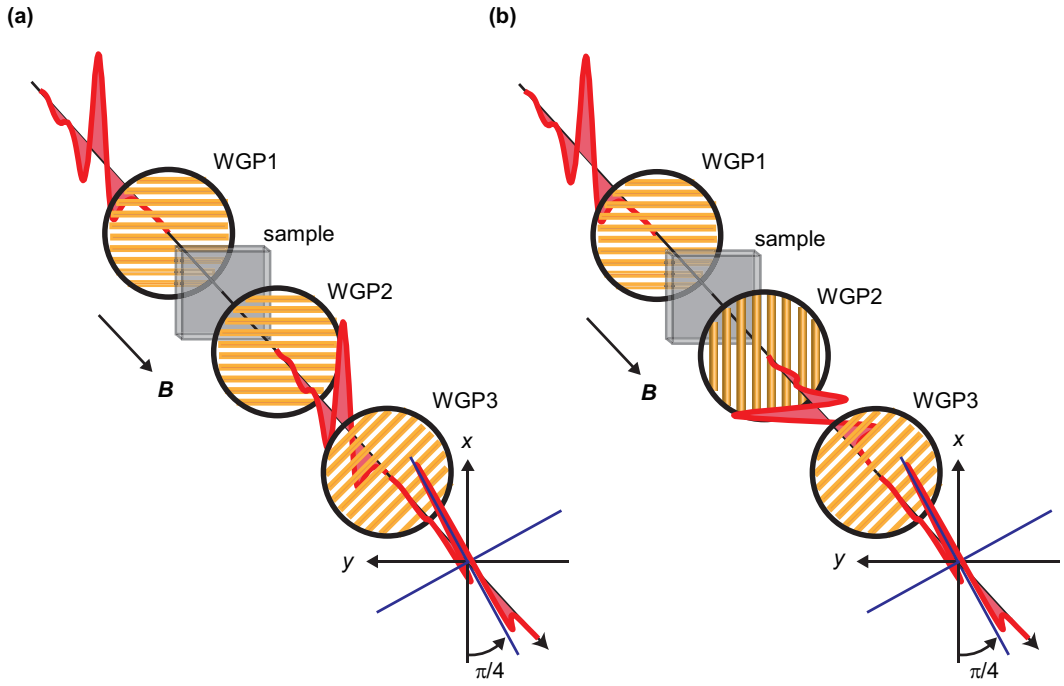

Figure 3.9: Configurations of wire-grid polarizers (WGPs) for the polarization-resolved THz detection in the case of the measurement of the transmitted THz electric field component parallel (a) or orthogonal (b) to the incident THz polarization.

uate the Faraday rotation angle and the ellipticity. We use three wire-grid polarizers (WGPs) for the polarization-resolved THz detection as shown in Fig. 3.9. Before the sample, we set a WGP, depicted as WGP1 in Fig. 3.9, to confirm that the incident THz pulse is linearly polarized in the x-direction. After the sample, we put two WGPs, which we call WGP2 and WGP3 hereinafter. WGP2 is set parallel (x) or orthogonal (y) to the incident THz polarization, as shown in Fig. 3.9 (a) and (b), respectively, so that only the x- or y-components of the transmitted THz pulse can transmit through WGP2 and be detected. After WGP2, we put WGP3 oriented at 45° to the incident THz polarization to fix the polarization dependence of THz detection resulting from the angle-dependent balanced detection signal explained in Eq. (3.15).

Because we need to measure the very small Faraday rotation angle on the order of mrad, the background signals have to be eliminated. Therefore, we measure $E_y^{\mathrm{t}}(t)$ at both the positive and the negative magnetic fields, $E_y^{\mathrm{t}}(+B)$ and $E_y^{\mathrm{t}}(-B)$, respectively, and subtract each other $E_y^{\mathrm{t}}(t) = (E_y^{\mathrm{t}}(+B) - E_y^{\mathrm{t}}(-B))/2$. Since the background signals do not change with respect to the sign reversal of the applied magnetic field, whereas Faraday rotation does change its sign, we can obtain the $E_y^{\mathrm{t}}(t)$ signal only from the sample.

Chapter 4

Contents in this chapter will be published in five years and are bot opened to the public now.
本章については、5 年以内に雑誌等で刊行予定のため、現在非公開。

Chapter 5

Contents in this chapter will be published in five years and are bot opened to the public now.
本章については、5 年以内に雑誌等で刊行予定のため、現在非公開。

Chapter 6

Contents in this chapter will be published in five years and are bot opened to the public now.
本章については、5 年以内に雑誌等で刊行予定のため、現在非公開。

Chapter 7

Contents in this chapter will be published in five years and are bot opened to the public now.
本章については、5 年以内に雑誌等で刊行予定のため、現在非公開。

References

[1] A. F. Young, and P. Kim, Quantum interference and Klein tunnelling in graphene heterojunctions. *Nature Phys.* **5,** 222-226 (2009).

[2] N. Stander, B. Huard, and D. Goldhaber-Gordon, Evidence for Klein Tunneling in Graphene p-n Junctions. *Phy. Rev. Lett.* **102,** 026807 (2009).

[3] K. S. Novoselov, A. K. Geim, S. V. Morozov, D. Jiang, M. I. Katsnelson, I. V. Grigorieva, S. V. Dubonos, and A. A. Firsov, Two-dimensional gas of massless Dirac fermions in graphene. *Nature* **438,** 197-200 (2005).

[4] Y. Zhang, Y. -W. Tan, H. L. Stormer, and P. Kim, Experimental observation of the quantum Hall effect and Berry's phase in graphene. *Nature* **438,** 201-204 (2005).

[5] F. Bonaccorso, Z. Sun, T. Hasan, and A. C. Ferrari, Graphene photonics and opto-electronics. *Nature Photon.* **4,** 611-622 (2010).

[6] A. N. Grigorenko, M. Polini, and K. S. Novoselov, Graphene plasmonics. *Nature Photon.* **6,** 749-758 (2012).

[7] E. Hendry, P. J. Hale, J. Moger, A. K. Savchenko, and S. A. Mikhailov, Coherent Nonlinear Optical Response of Graphene. *Phys. Rev. Lett.* **105,** 097401 (2010).

[8] J. L. Cheng, N. Vermeulen, and J. E. Sipe, Third order optical nonlinearity of graphene. *New J. Phys.* **16,** 053014 (2014).

[9] S. A. Mikhailov, and K. Ziegler, Nonlinear electromagnetic response of graphene: frequency multiplication and the self-consistent-field effects. *J. Phys. Condens. Matter* **20,** 384204 (2008).

[10] N. Kumar, J. Kumar, C. Gerstenkorn, R. Wang, H. -Y. Chiu, A. L. Smirl, and H. Zhao, Third harmonic generation in graphene and few-layer graphite films. *Phys. Rev. B* **87,** 121406 (2013).

[11] S. -Y. Hong, J. I. Dadap, N. Petrone, P. -C. Yeh, J. Hone, and R. M. Osgood, Optical third-harmonic generation in graphene. *Phys. Rev. X* **3,** 021014 (2013).

[12] K. L. Ishikawa, Nonlinear optical response of graphene in time domain. *Phys. Rev. B* **82,** 201402 (2010).

[13] I. A. -Naib, J. E. Sipe, and M. M. Dignam, High harmonic generation in undoped graphene: Interplay of inter- and intraband dynamics. *Phys. Rev. B* **90,** 245423 (2014).

[14] L. A. Chizhova, F. Libisch, and J. Burgdörfer, Nonlinear response of graphene to a few-cycle terahertz laser pulse: Role of doping and disorder. *Phys. Rev. B* **94,** 075412 (2016).

[15] P. Bowlan, E. Martinez-Moreno, K. Reimann, T. Elsaesser, and M. Woerner, Ultrafast terahertz response of multilayer graphene in the nonperturbative regime. *Phys. Rev. B* **89,** 041408 (2014).

[16] M. J. Paul, Y. C. Chang, Z. J. Thompson, A. Stickel, J. Wardini, H. Choi, E. D. Minot, B. Hou, J. A. Nees, T. B. Norris, and Y. -S. Lee, High-field terahertz response of graphene. *New J. Phys.* **15,** 085019 (2013).

[17] H. Y. Hwang, N. C. Brandt, H. Farhat, A. L. Hsu, J. Kong, and K. A. Nelson, Nonlinear THz Conductivity Dynamics in P-Type CVD-Grown Graphene. *J. Phys. Chem. B* **117,** 15819-15824 (2013).

[18] Z. Mics, K. -J. Tielrooij, K. Parvez, S. A. Jensen, I. Ivanov, X. Feng, K. Mullen, M. Bonn, and D. Turchinovich, Thermodynamic picture of ultrafast charge transport in graphene. *Nature Commun.* **6,** 7655 (2015).

[19] M. O. Goerbig, Electronic properties of graphene in a strong magnetic field. *Rev. Mod. Phys.* **83,** 1193-1243 (2011).

[20] I. Crassee, J. Levallois, A. L. Walter, M. Ostler, A. Bostwick, E. Rotenberg, T. Seyller, D. van der Marel, and A. B. Kuzmenko, Giant Faraday rotation in single- and multilayer graphene. *Nature Phys.* **7,** 48-51 (2010).

[21] R. Shimano, G. Yumoto, J. Y. Yoo, R. Matsunaga, S. Tanabe, H. Hibino, T. Morimoto, and H. Aoki, Quantum Faraday and Kerr rotations in graphene. *Nature Commun.* **4,** 1841 (2013).

[22] M. L. Sadowski, G. Martinez, M. Potemski, C. Berger, and W. A. de Heer, Landau Level Spectroscopy of Ultrathin Graphite Layers. *Phy. Rev. Lett.* **97,** 266405 (2006).

[23] L. G. Booshehri, C. H. Mielke, D. G. Rickel, S. A. Crooker, Q. Zhang, L. Ren, E. H. Hároz, A. Rustagi, C. J. Stanton, Z. Jin, Z. Sun, Z. Yan, J. M. Tour, and J. Kono, Circular polarization dependent cyclotron resonance in large-area graphene in ultrahigh magnetic fields. *Phys. Rev. B* **85,** 205407 (2012).

[24] M. Orlita, I. Crassee, C. Faugeras, A. B. Kuzmenko, F. Fromm, M. Ostler, Th. Seyller, G. Martinez, M. Polini, and M. Potemski, Classical to quantum crossover of the cyclotron resonance in graphene: a study of the strength of intraband absorption. *New J. Phys.* **14,** 095008 (2012).

[25] I. Crassee, J. Levallois, D. van der Marel, A. L. Walter, Th. Seyller, and A. B. Kuzmenko, Multicomponent magneto-optical conductivity of multilayer graphene on SiC. *Phys. Rev. B* **84,** 035103 (2011).

[26] I. Crassee, M. Orlita, M. Potemski, A. L. Walter, M. Ostler, T. Seyller, I. Gaponenko, J. Chen, and A. B. Kuzmenko, Intrinsic terahertz plasmons and magnetoplasmons in large scale monolayer graphene. *Nano Lett.* **12,** 2470-2474 (2012).

[27] P. Plochocka, P. Kossacki, A. Golnik, T. Kazimierczuk, C. Berger, W. A. de Heer, and M. Potemski, Slowing hot-carrier relaxation in graphene using a magnetic field. *Phys. Rev. B* **80,** 245415 (2009).

[28] M. Mittendorff, M. Orlita, M. Potemski, C. Berger, W. A. de Heer, H. Schneider, M. Helm, and S. Winnerl, Intraband carrier dynamics in Landau-quantized multilayer epitaxial graphene. *New J. Phys.* **16,** 123021 (2014).

[29] M. Mittendorff, F. Wendler, E. Malic, A. Knorr, M. Orlita, M. Potemski, C. Berger, W. A. de Heer, H. Schneider, M. Helm, and S. Winnerl, Carrier dynamics in Landau-quantized graphene featuring strong Auger scattering. *Nature Phys.* **11,** 75-81 (2015).

[30] D. Hagenmüller, S. De Liberato, and C. Ciuti, Ultrastrong coupling between a cavity resonator and the cyclotron transition of a two-dimensional electron gas in the case of an integer filling factor. *Phys. Rev. B* **81,** 235303 (2010).

[31] S. Hughes, Breakdown of the Area Theorem: Carrier-Wave Rabi Flopping of Femtosecond Optical Pulses. *Phys. Rev. Lett.* **81,** 3363-3366 (1998).

[32] F. Krausz, and M. Ivanov, Attosecond physics. *Rev. Mod. Phys.* **81,** 163-234 (2009).

[33] F. Junginger, B. Mayer, C. Schmidt, O. Schubert, S. Mährlein, A. Leitenstorfer, R. Huber, and A. Pashkin, Nonperturbative Interband Response of a Bulk InSb Semiconductor Driven Off Resonantly by Terahertz Electromagnetic Few-Cycle Pulses. *Phys. Rev. Lett.* **109,** 147403 (2012).

[34] S. Ghimire, A. D. DiChiara, E. Sistrunk, P. Agostini, L. F. DiMauro, and D. A. Reis, Observation of high-order harmonic generation in a bulk crystal. *Nature Phys.* **7,** 138-141 (2011).

[35] O. Schubert, M. Hohenleutner, F. Langer, B. Urbanek, C. Lange, U. Huttner, D. Golde, T. Meier, M. Kira, S. W. Koch, and R. Huber, Sub-cycle control of terahertz high-harmonic generation by dynamical Bloch oscillations. *Nature Photon.* **8,** 119-123 (2014).

[36] T. Maag, A. Bayer, S. Baierl, M. Hohenleutner, T. Korn, C. Schuller, D. Schuh, D. Bougeard, C. Lange, R. Huber, M. Mootz, J. E. Sipe, S. W. Koch, and M. Kira, Coherent cyclotron motion beyond Kohn's theorem. *Nature Phys.* **12,** 119-123 (2016).

[37] X. Yao, and A. Belyanin, Giant Optical Nonlinearity of Graphene in a Strong Magnetic Field. *Phy. Rev. Lett.* **108,** 255503 (2012).

[38] M. Tokman, X. Yao, and A. Belyanin, Generation of Entangled Photons in Graphene in a Strong Magnetic Field. *Phys. Rev. Lett.* **110,** 077404 (2013).

[39] H. K. Avetissian, and G. F. Mkrtchian, Coherent nonlinear optical response of graphene in the quantum Hall regime. *Phys. Rev. B* **94,** 045419 (2016).

[40] A. H. Castro Neto, N. M. R. Peres, K. S. Novoselov, and A. K. Geim, The electronic properties of graphene. *Rev. Mod. Phys.* **81,** 109-162 (2009).

[41] R. S. Deacon, K. C. Chuang, R. J. Nicholas, K. S. Novoselov, and A. K. Geim, Cyclotron resonance study of the electron and hole velocity in graphene monolayers. *Phys. Rev. B* **76,** 081406 (2007).

[42] X. Yao, and A. Belyanin, Nonlinear optics of graphene in a strong magnetic field. *J. Phys. Condens. Matter* **25,** 054203 (2013).

[43] Y. Zheng, T. Ando, Hall conductivity of a two-dimensional graphite system. *Phy. Rev. B* **65,** 245420 (2002).

[44] D. M. Mittleman, M. Gupta, R. Neelamani, R. G. Baraniuk, J. V. Rudd, and M. Koch, Recent advances in terahertz imaging. *Appl. Phys. B* **68,** 1085-1094 (1999).

[45] A. Nahata, A. S. Weling, and T. F. Heinz, A wideband coherent terahertz spectroscopy system using optical rectification and electro-optic sampling. *Appl. Phys. Lett.* **69,** 2321-2323 (1996).

[46] Q. Wu and X. -C. Zhang, 7 terahertz broadband GaP electro-optic sensor. *Appl. Phys. Lett.* **70,** 1784-1786 (1997).

[47] A. Leitenstorfer, S. Hunsche, J. Shah, M. C. Nuss, and W. H. Knox, Detectors and sources for ultrabroadband electro-optic sampling: Experiment and theory. *Appl. Phys. Lett.* **74,** 1516-1518 (1999).

[48] Q. Chen, M. Tani, Z. Jiang, and X. -C. Zhang, Electro-optic transceivers for terahertz-wave applications. *J. Opt. Soc. Am. B* **18,** 823-831 (2001).

[49] R. W. Boyd, *Nonlinear Optics*. Academic press, 3rd edition (2010).

[50] G. Gallot, and D. Grischkowsky, Electro-optic detection of terahertz radiation. *J. Opt. Soc. Am. B* **16,** 1204-1212 (1999).

[51] A. Yariv, and P. Yeh, *Photonics: optical electronics in modern communications*. Oxford university press, 6th edition (2006).

[52] K. W. Chiu, and T. K. Lee, Infrared magneto-transmittance of a two-dimensional electron gas. *Surf. Sci.* **58,** 182 (1976).

[53] H. Hibino, S. Tanabe, S. Mizuno, and H. Kageshima, Growth and electronic transport properties of epitaxial graphene on SiC. *J. Phys. D Appl. Phys.* **45,** 154008 (2012).

[54] D. S. Lee, C. Riedl, B. Krauss, K. von Klitzing, U. Starke, and J. H. Smet, Raman Spectra of Epitaxial Graphene on SiC and of Epitaxial Graphene Transferred to SiO2. *Nano Lett.* **8,** 4320-4325 (2008).

[55] X. Xie, J. Dai, and X. -C. Zhang, Coherent Control of THz Wave Generation in Ambient Air. *Phys. Rev. Lett.* **96,** 075005 (2006).

[56] M. Clerici, M. Peccianti, B. E. Schmidt, L. Caspani, M. Shalaby, M. Giguère, A. Lotti, A. Couairon, F. Légaré, T. Ozaki, D. Faccio, and R. Morandotti, Wavelength Scaling of Terahertz Generation by Gas Ionization. *Phys. Rev. Lett.* **110,** 253901 (2013).

[57] J. Dai, N. Karpowicz, and X. -C. Zhang, Coherent Polarization Control of Terahertz Waves Generated from Two-Color Laser-Induced Gas Plasma. *Phys. Rev. Lett.* **103,** 023001 (2009).

[58] S. Tani, F. Blanchard, and K. Tanaka, Ultrafast Carrier Dynamics in Graphene under a High Electric Field. *Phys. Rev. Lett.* **109,** 166603 (2012).

[59] J. Hebling, K. L. Yeh, M. C. Hoffmann, B. Bartal, and K. A. Nelson, Generation of high-power terahertz pulses by tilted-pulse-front excitation and their application possibilities. *J. Opt. Soc. Am. B* **25,** B6-B19 (2008).

[60] J. Hebling, A. G. Stepanov, G. Almási, B. Bartal, and J. Kuhl, Tunable THz pulse generation by optical rectification of ultrashort laser pulses with tilted pulse fronts. *Appl. Phys. B: Lasers Opt.* **78,** 593-599 (2004).

[61] J. Hebling, G. Almási, I. Z. Kozma, and J. Kuhl, Velocity matching by pulse front tilting for large-area THz-pulse generation. *Opt. Express* **10,** 1161-1166 (2002).

[62] H. Hirori, A. Doi, F. Blanchard, and K. Tanaka, Single-cycle terahertz pulses with amplitudes exceeding 1 MV/cm generated by optical rectification in LiNbO3. *Appl. Phys. Lett.* **98,** 091106 (2011).

[63] S. Watanabe, N. Minami, and R. Shimano, Intense terahertz pulse induced exciton generation in carbon nanotubes. *Opt. Express* **19,** 1528-1538 (2011).

[64] M. Dressel, and G. Grüner, *Electrodynamics of Solids: Optical Properties of Electrons in Matter*. Cambridge Univ. Press (2002).

[65] P. Bowlan, E. Martinez-Moreno, K. Reimann, M. Woerner, and T. Elsaesser, Terahertz radiative coupling and damping in multilayer graphene. *New J. Phys.* **16,** 013027 (2014).

[66] F. Wendler, A. Knorr, and E. Malic, Ultrafast carrier dynamics in Landau-quantized graphene. *Nanophotonics* **4,** 224 (2015).

[67] H. Funk, A. Knorr, F. Wendler, and E. Malic, Microscopic view on Landau level broadening mechanisms in graphene. *Phys. Rev. B* **92,** 205428 (2015).

[68] S. Piscanec, M. Lazzeri, F. Mauri, A. Ferrari, and J. Robertson, Kohn Anomalies and Electron-Phonon Interactions in Graphite. *Phy. Rev. Lett.* **93,** 185503 (2004).

[69] A. Ferreira, J. Viana-Gomes, Yu V. Bludov, V. Pereira, N. M. R. Peres, and A. H. Castro Neto, Faraday effect in graphene enclosed in an optical cavity and the equation of motion method for the study of magneto-optical transport in solids. *Phy. Rev. B* **84,** 235410 (2011).

[70] M. O. Scully, and M. S. Zubairy, *Quantum Optics*. Cambridge Univ. Press (1997).

[71] It has been reported that under the relatively weak monochromatic light irradiation, the OSE of the LLs is analytically examined: O. V. Kibis, S. Morina, K. Dini, and I. A. Shelykh, Magnetoelectronic properties of graphene dressed by a high-frequency field. *Phy. Rev. B* **93,** 115420 (2016).

[72] R. Matsunaga, N. Tsuji, H. Fujita, A. Sugioka, K. Makise, Y. Uzawa, H. Terai, Z. Wang, H. Aoki, and R. Shimano, Light-induced collective pseudospin precession resonating with Higgs mode in a superconductor. *Science* **345,** 1145-1149 (2014).

[73] H. Liu, Y. Li, Y. S. You, S. Ghimire, T. F. Heinz, and D. A. Reis, High-harmonic generation from an atomically thin semiconductor. *Nature Phys.* DOI: 10.1038/nphys3946 (2016).

Acknowledgments

In this very last part of my dissertation, I would like to express my sincere gratitude to those who have been encouraging me in my studies and helping me during my PhD years. First of all, I would like to thank my supervisor Prof. Ryo Shimano for giving me a lot of useful advices and taking time to help me with my writing and presentations. I would also like to say thank you to an assistant professor of our group Ryusuke Matsunaga for helping me with my studies by means of not only giving me useful scientific advices but also providing a great work environment. I would like to heartily thank my research collaborator Prof. Hiroki Hibino for providing us great graphene samples for terahertz measurements. I want to thank all of my group members, Fumiya Sekiguchi, Yuki I. Hamada, Masayuki Takayama, Keisuke Tomita, Kaito Tomari, Yuta Murotani, Kota Katsumi, and Takuya Sawano. I also want to say a big thank you to alumni of our group, especially to Takeshi Suzuki, Je-Yoon Yoo, Kazuhiro Shibagaki, and Takahiro Yamazaki. They all have been very gentle with me and gave me a wonderful PhD life. Besides, I would like to appreciate a financial support from JSPS and Advanced Leading Graduate Course for Photon Science. At last, I want to thank my friends and family for supporting me and cheering me up all the time.